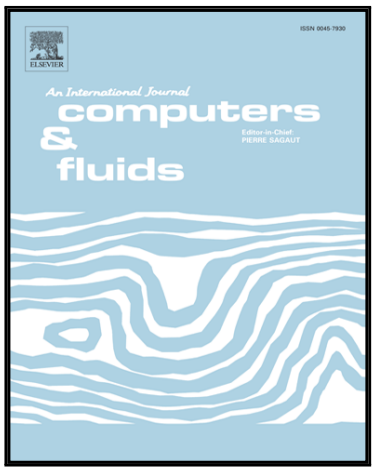

A parallel Volume of Fluid-Lagrangian Parcel Tracking coupling procedure for diesel spray modelling

H. Yu , L. Goldsworthy , M. Ghiji , P.A. Brandner , V. Garaniya

PII: S0045-7930(17)30108-1
DOI: 10.1016/j.compfluid.2017.03.027
Reference: CAF 3438

To appear in: *Computers and Fluids*

Received date: 23 November 2016
Revised date: 24 March 2017
Accepted date: 29 March 2017

Please cite this article as: H. Yu , L. Goldsworthy , M. Ghiji , P.A. Brandner , V. Garaniya , A parallel Volume of Fluid-Lagrangian Parcel Tracking coupling procedure for diesel spray modelling, *Computers and Fluids* (2017), doi: 10.1016/j.compfluid.2017.03.027

A parallel Volume of Fluid-Lagrangian Parcel Tracking coupling procedure for diesel spray modelling

H. Yu*, L. Goldsworthy, M. Ghiji, P.A. Brandner, V. Garaniya
Australian Maritime College, University of Tasmania, Launceston, Tasmania 7250

Abstract

A parallel computing Eulerian/Lagrangian multi-scale coupling procedure for diesel spray simulation is presented. Early breakup of the diesel jet is captured by using a compressible Volume of Fluid (VOF) method. In regions where the phase interface can no longer be sufficiently resolved, separated and small scale liquid structures are described by a Lagrangian Parcel Tracking (LPT) approach, in conjunction with secondary breakup modelling and a turbulence stochastic dispersion model. The coupling of these two descriptions utilises a Region Coupling Method and an efficiently parallelised droplet identification and extraction procedure. This approach enables run-time VOF-LPT field coupling and filters small-scale liquid structures that are suitable candidates for Eulerian-liquid-structure/Lagrangian droplet conversion, preserving their position, mass and momentum. The coupling procedure is initially applied to model the atomisation of a simple liquid jet and the results are compared with that of a statistical coupling approach to demonstrate the performance of the developed coupling procedure. Its application is then extended to simulate a real diesel spray from a nozzle with a sharp entrance. Coupling in-nozzle phenomena such as flow separation, flow detachment and turbulence to the primary and secondary spray atomisation, provides a tool for the prediction of complex spray dynamics.

Keywords: Eulerian (Volume of Fluid); Lagrangian (Lagrangian Parcel Tracking); Parallel coupling; Two-phase flows; Compressible flow; Diesel spray atomisation.

---

*Corresponding author.
Email address: hongjiang.yu@utas.edu.au (H. Yu)

ABBREVIATIONS

VOF Volume of Fluid

LPT Lagrangian Parcel Tracking

LES Large Eddy simulation

LSM Level Set Method

DCA Direct Coupling Approach

RCM Region Coupling Method

DIP Droplet Identification Procedure

DEP Droplet Extraction Procedure

SCA Statistical Coupling Approach

ASOI After Start of Injection

NOMENCLATURE

ρ Mixture density

U Velocity

P Pressure

t Time

τ Shear stress

σ Surface tension coefficient

α_l Liquid volume fraction

$\mathbb{n}$ Unit vector normal to the liquid surface

κ Liquid surface curvature

δ Dirac function

ρ_l Density of the liquid phase

ρ_g Density of the gas phase

ρ_0 Reference density for the liquid phase

ψ_l Compressibility of the liquid phase

ψ_g Compressibility of the gas phase

μ Mixture dynamic viscosity

μ_l Liquid phase dynamic viscosity

μ_g Gas phase dynamic viscosity

τ_{sgs} Sub-grid shear stress

k Sub grid kinetic energy

υ Kinetic viscosity

υ_{sgs} Sub-grid kinetic viscosity

ε Turbulent dissipation

h Enthalpy

h_{sgs} Sub-grid enthalpy

X_p Parcel position vector

U_p Parcel velocity vector

U_g Gas phase velocity vector

U_{rel} Relative velocity between parcel and gas

C_D Drag coefficient

Re_p Parcel Reynolds number

C Cavitation number

Re Mixture Reynolds number

d_p Parcel diameter

τ_p Parcel characteristic time

$\overline{S_U^s}$ Parcel momentum source term

λ Thermal diffusion

Z Mixture fraction

D Mass diffusion

T Temperature

$\Phi^Z{}_{sgs}$ Sub-grid species mass flux

m_p Mass of a parcel

V_{cell} Volume of a mesh cell

V_p Volume of a parcel

R_p Radius of a parcel

X_P Position vector of a parcel

X_{cell} Position vector of a cell

1. INTRODUCTION

Achieving an efficient combustion process in diesel engines requires optimally combined effects of air and fuel mixing, turbulence generation and interaction of spray and engine geometry. This involves improving the atomisation of the diesel spray by taking into account various operating conditions such as different nozzle designs, operating temperatures as well as the injection and chamber pressures. Many studies have focused on these aspects in an effort to realise more efficient combustion and reduced emissions [1].

In diesel engines, the fuel is injected at a high pressure into the combustion chamber where it follows a series of disintegration processes. Initially, the interaction between the fuel and nozzle geometry results in a flow regime dominated by separation, cavitation and aerodynamic instabilities causing primary jet break-up in the vicinity of the nozzle exit [1, 2]. In this process, the fragmentation of the intact liquid core generates large liquid structures that will undergo secondary breakup and further disintegrate into small droplets. At the next stage, the spacing between droplets increases further downstream of the nozzle due to air entrainment and turbulent droplet-gas interaction, and the droplet size decreases owing to secondary breakup and evaporation.

The primary and secondary breakup mechanisms have been extensively studied experimentally, see for example [3-7]. The use of different measuring techniques especially X-ray analysis of diesel sprays has provided comprehensive information on the liquid penetration, cross-sectional projected density distribution. The measurement of these parameters can help gain a qualitative understanding about the diesel spray evolution. However, the shot to shot variation of sprays makes it difficult to quantitatively capture the detailed features of the spray at different stages [4]. Therefore, to obtain information on the spatial and temporal spray evolution with high resolution, computational simulations are essential.

Due to the complex behaviour of the diesel spray in the primary and secondary atomisation processes, various computational approaches have been proposed and developed to simulate these. For primary atomisation, interface capturing/tracking methods such as the Volume of Fluid (VOF) method [8-14], Level Set Method (LSM) [15, 16] and the combination of both[17, 18] are widely adopted. In the VOF method, the liquid and gas are treated as two immiscible phases that are both described in the Eulerian framework. A transport equation calculating the volume fraction of each phase in a cell is employed and the derived gradient of the volume fraction of the dense phase is used to construct the liquid interface. This intrinsically allows the simulation of jet breakup, liquid core disintegration and droplet coalescence in a volume conservative manner. However, sufficiently discretising all small scale liquid structures can lead to exponential increase in mesh elements, leading to excessive demand in computational time for complex two-phase flow cases. In the secondary atomisation, due to the increasingly dominant effect of surface tension on small scales, small liquid structures start to become either spherical or elliptical, and they fall in the framework of LPT. However, in order for these small structures to be valid for Lagrangian modelling, they need to be smaller than the grid size. To ensure numerical stability, the maximum size of particles is recommended to be smaller than 20% of the local grid size for Lagrangian particle tracking [19, 20]. This is one of the main limitations of the Lagrangian modelling that grid size could be larger than what might be desirable for good resolution of small scale flow features. A wide range of Lagrangian models have been developed specifically for the modelling of spray atomisation. Most of these are based on the Lagrangian description of individual droplets or parcels with an additional level of modelling for the primary and secondary atomisation [21-30]. The comparison of four different atomisation models, namely the Wave model [31], the Huh and Gosman atomisation model [32] and the MPI-1 and MPI-2 atomisation models is detailed in [33]. One of the drawbacks of these models is the lack of

detailed attention to the effects of in nozzle flow phenomena (e.g. flow separation, cavitation and turbulence), resulting in the inaccurate prediction of primary spray breakup. However, they possess the advantage that it is rather efficient to simulate the evolution of a cluster of small-scale liquid structures without a high demand in computational time. This is enabled by the use of many well-developed secondary breakup models. Typically, the KH model by Reitz [23] as one of the earliest developed droplet breakup models predicts the development of aerodynamically induced disturbances on the liquid surface employing the Kelvin-Helmholtz (KH) mechanism. This mechanism relates the radii of parent and child parcels with the fastest growing wave length on the liquid surface and its corresponding growth rate. The RT model by Amsden *et al.* [34], on the other hand, describes Rayleigh-Taylor instabilities growing on a liquid-gas interface due to the density jump between gas and liquid. A parameter known as the break up time is introduced in this model, and it acts as a trigger to initiate the breakup process when the growing time of RT waves on the droplet surface is greater than the break up time. A hybrid model combining the KH and RT models is then developed to account for both the primary and secondary breakup of jets using a switching threshold Weber Number We = 12 [35].

In the light of the development of various primary and secondary atomisation modelling approaches, many attempts have been made to combine the merits of interface tracking/capturing and Lagrangian particle tracking. One of the first Interface-Tracking/Point Particle Tracking coupling procedures for jet breakup simulation is reported by Hermann *et al.* [36]. A dual grid method in which Eulerian (Level Set) and Lagrangian (point particle tracking) descriptions of liquid spray are handled respectively on two individual grids with two-way momentum coupling was first introduced in spray modelling. A similar approach however with adaptive mesh refinement capability is demonstrated by Tomar *et al.* [37] where the liquid interface is captured by using a local mesh refinement algorithm and small

droplets are tracked as Lagrangian spherical particles in the region where the mesh is sufficiently coarse. Both approaches identify liquid structures having a volume smaller than a predefined threshold value from the Eulerian simulation and transfer them into individual particles eligible for particle tracking. These methods are often referred to as the Direct Coupling Approach (DCA) and provide unique ways to deal with mesh inconsistency problems encountered in simultaneous modelling of primary and secondary spray atomisation. One of the main drawbacks of DCA is the limitation that droplets generated from Eulerian simulation can only be expensively tracked as individual particles due to the absence of secondary breakup modelling. This is either because the exclusive use of velocity field information in the Eulerian-Lagrangian coupling disables the use of a secondary breakup model [36] or the computational power is insufficient for the integration of an adaptive mesh refinement method with secondary breakup modelling [37]. Consequently, applications of these approaches are limited to capturing only a small segment of the liquid jet breakup process (e.g. only 30 μs after start of injection in Hermann *et al.* [36] and five days for one unit time in Tomar *et al*. [37]). On the other hand, the secondary breakup models, typically the KH-RT model, can group fluid particles of similar properties in a limited number of parcels. The use of the parcel concept can ease the computational strain by reducing the number of individual particles tracked in the Lagrangian modelling of the spray. Without the parcel assumption, the application of the DCA methods to detailed study of complex multiphase flows is computationally restricted. Alternatively, the development and implementation of a Eulerian-Lagrangian Spray Atomisation (ELSA) model attributed to Burluka *et al*. [38] and Desportes *et al.* [39] effectively integrated the Lagrangian parcel tracking with a single phase Eulerian model. However, this model treats liquid and gas as a single phase mixture, hence the surface tension effect is not accounted for. The evaluation of mean size of the liquid ligaments is determined only by solving a transport equation for

liquid/gas interface density. More recent developments in spray modelling give rise to many mathematical approximations that statistically couple the primary and secondary atomisation processes. A representative study conducted by Grosshans *et al.* [40] presents the use of a coupling layer located within the region where the transition from primary to secondary atomisation occurs. The volume, velocity and position of liquid structures are sampled on the coupling layer in the Eulerian frame work till statistical convergence is achieved. Sampled data are then implemented as initial conditions with the parcel assumption for the subsequent modelling of secondary atomisation in a Lagrangian reference. In contrast, the probability density functions of the droplet size were extracted from the entire Eulerian domain by Befrui *et al.* [41] and the sampled size distribution data were used to reinitialise the spray simulation using the Lagrangian parcel tracking method. The statistical coupling procedures are advantageous in terms of efficiency and have relatively higher accuracy as compared to the pure Lagrangian description of the liquid spray. However, the stochastic way in which data are sampled and initialized for the second stage of spray modelling inevitably compromises the flow information supplied by the more accurate Eulerian modelling of the in-nozzle and near-nozzle flow. Also, their applications are limited to modelling static sprays due to the fact that the primary and secondary sprays are not directly coupled.

The objective of this study is therefore to advance the recent work on Eulerian/Lagrangian coupling [10, 36, 40, 41], using an open source finite volume tool OpenFOAM, by (1) development of a parallel processing procedure for the identification and extraction of droplets from VOF simulation and injecting them in the LPT framework, (2) development of a conservative transient region coupling procedure that allows runtime exchange of fluid information between VOF and LPT in the region where Eulerian-Lagrangian transition occurs, (3) integration of a sub-grid stochastic turbulent droplet dispersion model to improve the capability of an existing Lagrangian solver in OpenFoam

and (4) allowing the modelling of the secondary breakup of large droplets extracted from the VOF simulation and the generation and tracking of child parcels in the LPT simulation. The developed code enables simulation for the complete evolution of the transient diesel spray from in-nozzle flow to atomised droplets.

2. NUMERICAL METHODS

2.1. Region Coupling Method

One of the most challenging problems in diesel spray simulation is the different scales with which the continuous phase and the dispersed phase are modelled. Specifically, the primary breakup of the liquid jet requires a refined grid to capture the surface instabilities which generate large ligaments. These ligaments further interact with surrounding gases to produce smaller liquid structures (droplets) which are rather expensive to be discretised by an even finer grid. They fall in the Lagrangian reference that entails a coarse grid typically 5 times the size of droplets [19, 20]. This mesh inconsistency problem has been tackled either by a dual grid approach [10, 36] or a statistical coupling [40, 41] with the former being more accurate and the latter being more computationally efficient. The dual grid approach uses two entirely overlapping grids of different resolution, between which the exchange of momentum is performed with a conservative interpolation scheme [16]. However, due to the discrepancy in resolution between the two grids, the loss of background flow information is inevitable in the interpolation process. This problem is more severe in most statistical coupling approaches, which utilise statistically converged data sampled from the Eulerian simulation to initialise the Lagrangian simulation. The Region Coupling Method (RCM) described in this section overcomes the problems of both approaches.

The RCM employs two grids that are only partially overlapping. It enables regional coupling of an Eulerian liquid-Eulerian gas (VOF) regime with an Eulerian gas-Lagrangian droplets (LPT) regime. The coupling is performed by interpolating field information between

the liquid-gas mixture in the VOF simulation and the carrier phase (gas) in the LPT simulation. After receiving field information from the VOF simulation, the two-way interaction of the carrier phase and droplets is handled in the LPT simulation. The effects of the droplet dynamics on the carrier phase is then reflected on the VOF simulation through the two-way field interpolation process. The overlapping region is where the transition from primary to secondary spray atomisation occurs and it couples the VOF and LPT simulations with two identical overlapping grids. Figure 1 shows the position of this region in relation to the spray. The developing spray is divided into three stages, namely the primary breakup stage when an intact liquid core is present, the transition stage (dense region) at which the liquid core starts to disintegrate into large ligaments and finally the diluted phase in which small liquid structures form and are dispersed by the carrier phase. It should be mentioned that the right end of the coupling region should be placed far away from the maximum liquid penetration to avoid potential boundary effects and to prevent unconverted VOF droplets from escaping the domain.

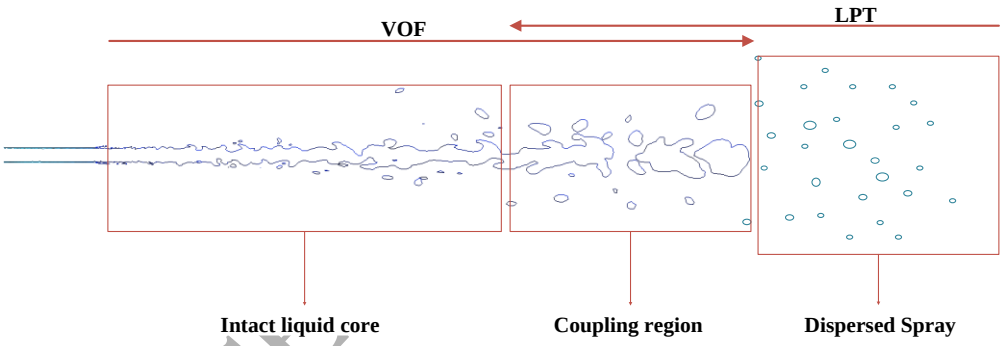

Figure 1: Region VOF-LPT coupling for a liquid diesel spray. The RCM is employed in the coupling region where VOF and LPT overlap.

One disadvantage of the RCM is that a decision has to be made as to where to place the overlap region, which requires that the Eulerian code needs to first be run till the liquid penetration reaches maximum within a predefined injection period. The maximum liquid

penetration is defined at the furthest point (along the penetration) where a grid cell has a liquid volume fraction (α_l) greater than 0.05.

However, a relatively coarse mesh can be employed with the VOF method to estimate the maximum liquid penetration. Alternatively, the use of generic experimental data can also help determine the extent of a diesel spray by using the Musculus and Kattke model [42], for example. The present study utilises an incremental method where the VOF domain is gradually extended to accommodate the maximum liquid penetration. This is achieved through expanding the VOF computational domain incrementally along the penetration and reinitialising the simulation with the new domain by mapping the field data from the previous simulation. In this process, the time and location at which major breakup of the liquid core occurs are also determined. After the maximum liquid penetration has been estimated, the coupling region should be placed to encompass the entire dense (major breakup) region that encompasses most large ligaments. Also, the end of the VOF/coupling region is placed far away from the maximum penetration to allow flow recirculation and avoid pressure reflection. The latter is achieved by employing a non-reflective boundary condition at the end of the VOF domain. The same grid generation strategy is also applied in the direction perpendicular to the penetration. This prevents all liquid structures from escaping the domain.

In the coupling region, it is computationally difficult to sufficiently describe all liquid structures of different scales using a refined grid with the VOF method. Therefore, the mesh resolution is progressively coarsened along the penetration of the liquid jet. The transition from a fine grid to a relatively coarse grid corresponds to the transition from VOF to LPT. The transition from VOF to LPT results in the decrease in the number of mesh elements that can be used to capture the interface of a liquid structure. At some points, the interface of the generated liquid structures can no longer be sufficiently resolved by the VOF method. These liquid structures are identified and converted to Lagrangian droplets if their volumes are

sufficiently smaller than the local cells in which their centroids lie. Therefore, a Droplet Identification Procedure (DIP) and a Droplet Extraction Procedure (DEP) comparing the volume of a liquid structure with the volume of a local cell containing this structure's centroid are developed. The code automatically adapts to the grid and frees users from defining a fixed threshold volume. It allows a greater variety of droplet diameters with a non-uniform grid than a uniform one. However, a threshold percentage determining the amount by which a liquid structure is smaller than its host cell needs to be defined. In this study, a liquid structure is recognised as a suitable Lagrangian droplet candidate if it has a volume smaller than 20% of the host cell's volume in the coupling region, as suggested in Arlov *et al.* [19].

The droplet conversion procedure enables the use of identical grids for both the VOF and LPT simulations in the coupling region. It solves the mesh inconsistency problem and allows high fidelity field coupling between VOF and LPT as the field mapping can be performed between two identical grids. Since interpolating field information between two identical grids produces negligible dissipation especially in mapping sub-scale kinetic energy, this method is independent of the turbulence model used. On the other hand, Large Eddy Simulation is chosen as the closure model for the governing equations in the present study. It is a less computationally intensive alternative to Direct Numerical Simulation and offers better ability to reflect the effects of local turbulence on the evolution of the bulk flow than the Reynolds averaged governing equations. However, it is only used to demonstrate the ability of the coupling procedure to model a transient diesel spray. The grid resolution is not necessarily fine enough for high resolution LES throughout the entire computational domain.

To reduce the computational intensity, the DIP and DEP as well as the two-way field mapping between VOF and LPT are deployed only in the coupling region. The two-way field mapping uses a volume conservative coupling algorithm taken from the parallel map-Fields

utility of OpenFOAM [43], known as cellVolumeWeight. It is a volume averaging algorithm that allows cell to cell conservative mapping of vector and scalar fields between two grids.

2.2. VOF

The VOF employed in the present study is based on a mathematical model composed of governing equations for the conservation of mass and momentum of a two-phase system, accredited to E. De Villiers *et al.* [44]. This system comprises two immiscible, compressible fluids and accounts for the surface tension between the two-phases. The single set of mass and momentum transport equations are:

$$\frac{\partial \rho}{\partial t} + \nabla \cdot (\rho U) = 0 \tag{1}$$

$$\frac{\partial \rho U}{\partial t} + \nabla \cdot (\rho U \bullet U) = -\nabla p + \nabla \cdot \tau + \int_{S(t)} \sigma \kappa n \cdot \delta (x - x') ds \tag{2}$$

where U is the velocity and ρ is the mixture density. The mixture density ρ is closely related to the local volume fraction α of each phase with $\alpha = 1$ representing a computational cell fully filled with liquid, while $\alpha = 0$ indicates a cell entirely occupied by gas. Any cell having $0 < \alpha < 1$ contains an interface segregating liquid and gas. For liquid-gas calculations, the mixture density in each computational unit is obtained from:

$$\rho = \alpha_l \rho_l + (1 - \alpha_l) \rho_g \tag{3}$$

where α_l is the volume fraction of liquid phase, ρ_l and ρ_g are the respective liquid and gas densities.

The integral term in equation (2) is a Dirac function that only produces a non-zero value when $x = x'$ which is an indication of the existence of a liquid interface. This source term accounts for the effect of surface tension force on the liquid jet breakup process. The evaluation of this term is achieved following E. De Villiers *et al.* [44] through the continuum surface force model of Brackbill *et al.* [45] as:

$$\int_{S(t)} \sigma n\kappa \cdot \delta\left(x - x^{'}\right) ds \approx \sigma\kappa\nabla\alpha \tag{4}$$

where σ is the surface tension coefficient, α is the volume fraction of the liquid phase which is obtained from the solution of a transport equation:

$$\frac{\partial \rho\alpha}{\partial t} + \nabla \cdot \left(\rho U\alpha\right) = 0 \tag{5}$$

and *n* is a unit vector normal to the liquid surface, κ is the interface curvature calculated from the solution of liquid phase volume fraction α :

$$\kappa = \nabla \cdot \left(\frac{\nabla\alpha}{|\nabla\alpha|}\right) \tag{6}$$

The system of equations is closed by an equation of state:

$$\begin{cases} \rho_l = \rho_0 + p\psi_l \\ \rho_g = p\psi_g \end{cases} \tag{7}$$

with ψ_l and ψ_l being the compressibility for liquid and gas phases respectively. The dynamic viscosity of the mixture is obtained through:

$$\mu = \alpha_l\mu_l + \left(1-\alpha_l\right)\mu_g \tag{8}$$

The VOF interface tracking method is a simple and flexible approach for the prediction of two-phase flows. A major limitation of this method is its limited ability to ensure boundedness of liquid volume fraction and preserve sharp interfaces without an interface reconstruction algorithm such as Piecewise Linear Interface Construction (PLIC) [46]. In the context of OpenFOAM, this problem is tackled with a 'Multi-Dimensional Universal Limiter with Explicit Solution" (MULES) accredited to Henry Weller together with the CICSAM interface compression scheme [47]. However, the numerical instabilities due to unboundedness of liquid volume fraction are not fully eliminated. Alternatively, high resolution prediction of flow with a free liquid surface can be achieved by local (Adaptive

Mesh Refinement [37]) or global grid refinement [48]. The present study adopts a globally refined grid for the VOF simulation. Another limitation of the current compressible VOF method is that the generated gas at low pressure sites is given the properties of air due to the lack of a phase change model. The generation of gas is primarily due to the flow separation downstream of the sharp nozzle inlet. The flow separation causes detachment of liquid from the wall and gas has to be introduced to satisfy the unity volume fraction ($\alpha_l + \alpha_g = 1$) under a two phase flow regime. This gas does not condense back to liquid fuel when the local pressure recovers above the vapour pressure. The incondensable gas then accumulates along the wall, causing complete detachment of liquid from the nozzle wall (hydraulic flip).

The LES model is integrated in equations (1), (2) and (4) through a local volume averaging procedure that decomposes relevant phase-weighted hydrodynamic variables into resolvable and sub-grid scale components. The elimination of the sub-grid fluctuations from direct simulation is done through a filtering process together with the non-linear convective terms in equation (2). This process generates additional terms comprising correlation of sub-scale variables that entail closure through additional modelling. Of these terms, the most crucial one is the Sub-Grid-Scale (SGS) stress that governs the effect of unresolved turbulence scales on momentum transport process and its dissipation. This term is defined as:

$$\tau_{sgs} = \overline{U \cdot U} - \overline{U} \cdot \overline{U} \tag{9}$$

The closure of the SGS stress is achieved through a sub-grid eddy viscosity model given as

$$\tau_{sgs} + \frac{\mu_{sgs}}{\rho}\left(\nabla \overline{U} + \nabla \overline{U}^{T}\right) = \frac{2}{3} kI \tag{10}$$

in which k is the SGS turbulence kinetic energy and μ_{sgs} is the SGS turbulent viscosity. These SGS turbulence parameters are calculated by using a one-Equation eddy model for evaluating k attributed to Yoshizawa [49].

$$\frac{\partial k}{\partial t}+\nabla\cdot\left(k\overline{U}\right)-\nabla\cdot\left[\left(\upsilon+\upsilon_{sgs}\right)\nabla k\right]=-\frac{1}{2}\tau_{sgs}:\left(\nabla\overline{U}+\nabla\overline{U}^{T}\right)-\varepsilon \tag{11}$$

where $\varepsilon=C_{\varepsilon}k^{(3/2)}/\Delta$ is the turbulent dissipation, $\upsilon_{sgs}=C_{k}k^{(1/2)}\Delta$ is the SGS kinematic viscosity ($\Delta=\sqrt[3]{V}$ represents the SGS length scale in which V represents the volume of the computational cell under consideration). The turbulent coefficients found from statistical analyses are $C_{k}=0.07$ and $C_{\varepsilon}=1.05$ [49]. As the emphasis of this study is placed mainly on obtaining reasonable resolution of spray simulation and the current implementation of LES is sufficient for this purpose, other SGS terms pertaining to density, mass transfer, phase fraction and surface tension are neglected.

2.3. LPT

The LPT method is derived based on the consideration of momentum exchange between the gas phase and the dispersed liquid phase, which is primarily described in the work of Jangi *et al.* [26]. This is achieved through the inclusion of additional source terms for the exchange rate of mass ($S_{\rho}^{s}=S_{Z}^{s}$), momentum (S_{U}^{s}) and heat (S_{h}^{s}) between the two phases in the gas phase governing equations, while the dynamics of the liquid phase are handled by Newton's second law. The evaporation of fuel is not considered in the present study as the spray is modelled at room temperature, therefore S_{ρ}^{s} and S_{Z}^{s} are assumed to be zero. The Favre-filtered LES conservation equations for the gas phase can be expressed as

$$\frac{\partial\overline{\rho}}{\partial t}+\nabla\cdot\left(\rho U\right)=\overline{S_{\rho}^{s}}=0 \tag{12}$$

$$\frac{\partial\overline{\rho}U}{\partial t}+\nabla\cdot\left[\overline{\rho}UU-\overline{\tau}+\tau_{sgs}\right]=\overline{S_{U}^{s}} \tag{13}$$

$$\frac{\partial\overline{\rho}h}{\partial t}+\nabla\cdot\left(\overline{\rho}Uh\right)-\nabla\cdot\left[\overline{\lambda}\nabla\cdot T+h_{sgs}\right]=\overline{S_{h}^{s}} \tag{14}$$

$$\frac{\partial \overline{\rho} Z}{\partial t} + \nabla \cdot \left(\overline{\rho} U Z \right) - \nabla \cdot \left[\overline{\rho D} \nabla \cdot Z + \Phi^{Z}{}_{sgs} \right] = \overline{S_Z^s} = 0 \tag{15}$$

The over-line signifies the general filtering

$$\overline{\phi(x,t)} = \int G(r,x)\phi(x-r,t)dr \tag{16}$$

where the integration is applied to the entire field with the filtering function satisfying the normalization condition

$$\int G(r,x)dr = 1 \tag{17}$$

The tilde represents the Favre filtering

$$\overline{\rho\phi} = \overline{\rho} \cdot \phi \tag{18}$$

in which ϕ is a dependant fluid field variable.

Apart from general fluid parameters, enthalpy h , thermal diffusion coefficient λ , mass diffusion coefficient D , mixture fraction Z and SGS species mass fluxes $\Phi^{Z}{}_{sgs}$ can be introduced to account for energy exchange and to ensure conservation. While the one-equation eddy model can be utilised to estimate the SGS stress term τ_{sgs} , the additional terms h_{sgs} and $\Phi^{Z}{}_{sgs}$ entail closure in order to close equations (14)-(15). They are modelled using a gradient diffusion-closure:

$$h_{sgs} = -\overline{\rho C_p} \frac{\upsilon_{sgs}}{\mathrm{Pr}^{sgs}} \nabla \cdot T \tag{19}$$

$$\Phi^{Z}{}_{sgs} = -\rho \frac{\upsilon^{sgs}}{Sc^{sgs}} \nabla \cdot Z \tag{20}$$

In Lagrangian spray simulation, the spray is considered as a discrete phase comprising a large quantity of parcels that are transported using Newtown's second law. The LPT method then provides closure for the source terms $\overline{S_U^s}$ in equation (13). The dynamics equations of the dispersed liquid phase are expressed as:

$$\frac{d}{dt}X_P = U_P \tag{21}$$

$$\frac{d}{dt}U_P = \frac{C_D}{\tau_P}\frac{\mathrm{Re}_P}{24}\left(U_g - U_P\right) = \frac{C_D}{\tau_P}\frac{\mathrm{Re}_P}{24}U_{rel} \tag{22}$$

and the drag coefficient is estimated as:

$$\begin{cases} C_D = \dfrac{24}{\mathrm{Re}_P}\left(1+\dfrac{1}{6}\mathrm{Re}_P^{2/3}\right) & \mathrm{Re}_P < 1000 \\ C_D = 0.424 & \mathrm{Re}_P \geq 1000 \end{cases} \tag{23}$$

Here X_P is the parcel position vector and U_p is the parcel velocity vector. The relative velocity U_{rel} between the parcel and the surrounding gases is denoted as $U_g - U_P$. For simplicity, the interaction between liquid and gas phases is accounted for by considering only the gravity and drag forces experienced by each parcel. The calculation of this force is given in equations (23) where the parcel Reynolds number is expressed as $\mathrm{Re}_P = \rho_g |U_{rel}| d_P / \mu_g$ with ρ_g being the density of gas phase, d_P being the parcel diameter and μ_g being the gas phase dynamic viscosity. $\tau_P = \rho_P d_P{}^2 / 18\mu_g$ is the time taken for a parcel to respond to local disturbances, also known as the parcel characteristic time. The instantaneous local velocity difference U_{rel} cannot be directly evaluated and requires closure. The current study employs O'Rourke's stochastic turbulence dispersion (STD) model [50] to estimate U_{rel} which, in LES formulation, can be written as:

$$U_{rel} = U + U_P^{'} - U_p \tag{24}$$

where U can be obtained by solving equation (13) and $U_P^{'}$ is the stochastic velocity vector accounting for the localised dispersion of parcels through the interaction with gases. $U_P^{'}$ is assumed to satisfy a Gaussian distribution with the variance $\sigma = \sqrt{2k_{sgs}/3}$ and the mean of

zero. In this way, the Gaussian distribution $G(U_{P,i}^{'}) = 1/\sigma\sqrt{2\pi}\exp\left(-U_{P,i}^{'}/2\sigma\right)^2$ randomly assigns values to each component of $U_P^{'}$ at every integration step of the gas (Eulerian) phase. In each computational cell, the momentum source term in equation (14) can be then obtained from:

$$\overline{S_U^s} = \frac{1}{V_{cell}}\sum\frac{d}{dt}\left(m_p U_{P,i}\right) \tag{25}$$

in which m_p is the mass of parcels under consideration and the summation is over all parcels existing in a computational cell having a volume of V_{cell}.

2.4. Secondary breakup model

According to Solsjö *et al.* [51], it is reasonable to assume that Kelvin-Helmholtz (KH) and Rayleigh-Taylor (RT) instabilities can occur simultaneously in the secondary breakup regime due to the high injection velocity. The KH-RT breakup model is therefore utilised to predict the atomisation process of secondary droplets in the LPT-LES simulation. In the present study, the KH-RT model allows the generation of parcels from the breakup of the large Lagrangian droplets (parent droplets) converted from the VOF liquid structures. Specifically, the diameters of the generated parcels (which are also referred to as child parcels) are determined by the KH-RT model after the breakup of the parent droplets. The number of fluid particles a child parcel contains is then determined by ensuring mass conservation before and after the secondary breakup of a parent droplet. Further details of the implementation of the KH-RT breakup model as well as the model constants ($B_0 = 0.61, B_1 = 10, C_{RT} = 0.1, C_\tau = 1$) used in this study can be found in Kitaguchi *et al.* [52].

2.5. Collision model

The collision of parcels is handled by a Stochastic Trajectory Collision (STC) model [53]. Unlike the O'Rourke collision model [54] which initiates collision of two parcels when they occupy the same computational cell and their estimated probability of collision is higher than a threshold value, the STC model takes the trajectory of each participant into account. This model considers the onset of collision between two parcels when their trajectories intersect, and the intersection point is reached at the same time within one Eulerian integration step.

2.6. Droplet Identification Procedure (DIP)

In this section, the development of a parallel droplet identification procedure is described. This procedure is designed to identify liquid structures that are smaller than 20% of their host cell's volume. In addition, it is determined that these liquid structures should be discretised by less than 5 mesh cells in order to minimise the effect of droplet eccentricity. Specifically, in the case that a small liquid structure satisfies the maximum volume criterion for VOF-LPT conversion and is spread over 5 or more mesh elements, it can have rather high eccentricity as depicted in Figure 2. Extracting such a liquid ligament and representing it with a spherical droplet in the LPT simulation can be a significant source of error especially for sub-grid physics. Therefore, only liquid structures that satisfy the minimum volume requirement and are discretised by less than 5 elements are considered eligible candidates for VOF-LPT conversion. Further, only identifying and extracting liquid structures occupying less than 5 mesh elements is computationally advantageous that such a process is not implemented on all large scale liquid structures which are dominant in the VOF simulation.

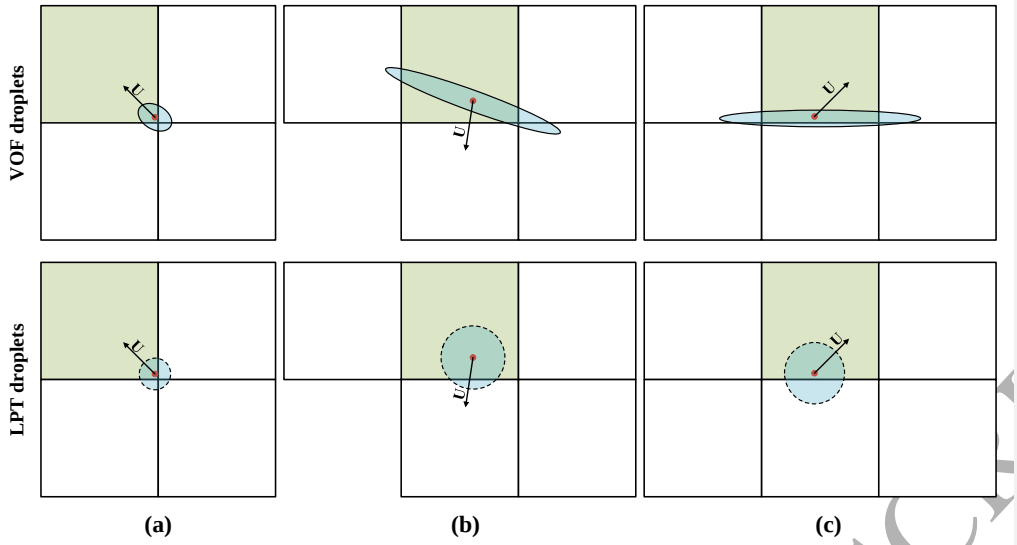

Figure 2: Three moving liquid structures having a velocity vector U and a volume smaller than 20% of their host cell (shaded in green) are captured by 4 mesh cells (a), 5 mesh cells (b) and 6 mesh cells (c) in the VOF domain. After a volume conservative conversion to LPT droplets, they are represented with spherical droplets at the same location in the LPT domain.

In the context of OpenFOAM, field values such as velocity, pressure, temperature and liquid volume fraction (∂_l) are stored at the centre of the controlled volumes (mesh cells). The interpolation of the cell-centred values to the face centres based on the face flux (advection) and values in neighbouring cells is fundamental to the finite volume method. The interpolation methods and schemes are detailed in Rusche [55]. In the present study, the identification process involves grouping adjacent liquid-containing cells ($\partial_l \geq 0.05$) sharing one cell face which has a liquid volume fraction $\partial_l \geq 0.05$ to form contiguous liquid structures. The reason for the selection of $\alpha_l = 0.05$ is to minimise the numerical instabilities introduced by the unboundedness of liquid volume fraction in each computational cell. The unboundedness of liquid volume fraction means that a cell with $\alpha_l \approx 0$ could have a α_l fluctuating between 0 and 10^{-6} depending on the solver's precision. For mesh cells with relative poor orthogonal quality, the range of fluctuation can become larger (10^{-3}) depending on the temporal resolution and number of corrections in the MULES loop. The use of a

smaller liquid volume threshold can result in the generation of a large number of physically unrealistic small droplets mainly due to oscillation of liquid volume fraction. This does not ensure mass conservation in the VOF-LPT conversion process. On the other hand, using a larger threshold can lead to the negligence of a considerable amount of small liquid structures that have a volume fraction slightly higher than 0.05. Allowing these droplets to be continuously modelled by the VOF method constitutes a significant source of error for the modelling of sub-grid physics in the VOF simulation. Moreover, the identification method is slower with the use of a smaller threshold liquid volume fraction. Typically, using $\partial_l = 0$ can result in the increase in computational time by an order of magnitude compared to that of $\partial_l \geq 0.05$.

In the developed procedure, the identified contiguous structures' velocities (U_P), centroids (x_P) and equivalent spherical diameters (R_p) are evaluated as:

$$V_p = \sum_N \alpha_l V_{cell} \tag{26}$$

$$R_p = \frac{1}{2}\left(\frac{6V_P}{\pi}\right)^{\frac{1}{3}} \tag{27}$$

$$X_P = \frac{1}{V_P}\sum_N X_{cell}\alpha_l V_{cell} \tag{28}$$

$$U_P = \frac{1}{V_P}\sum_N U_l \alpha_l V_{cell} \tag{29}$$

Hereafter *N* is the total number of adjacent computational cells with a liquid volume fraction greater than 0.05. The summation is over all identified mesh cells that belong to a complete liquid structure. The identification process is shown in Figure 3(a). To ensure the uniqueness of every liquid structure across the entire domain, the next step is to update the IDs of all liquid structures according to the rank of their host processor, as depicted in Figure 3(b).

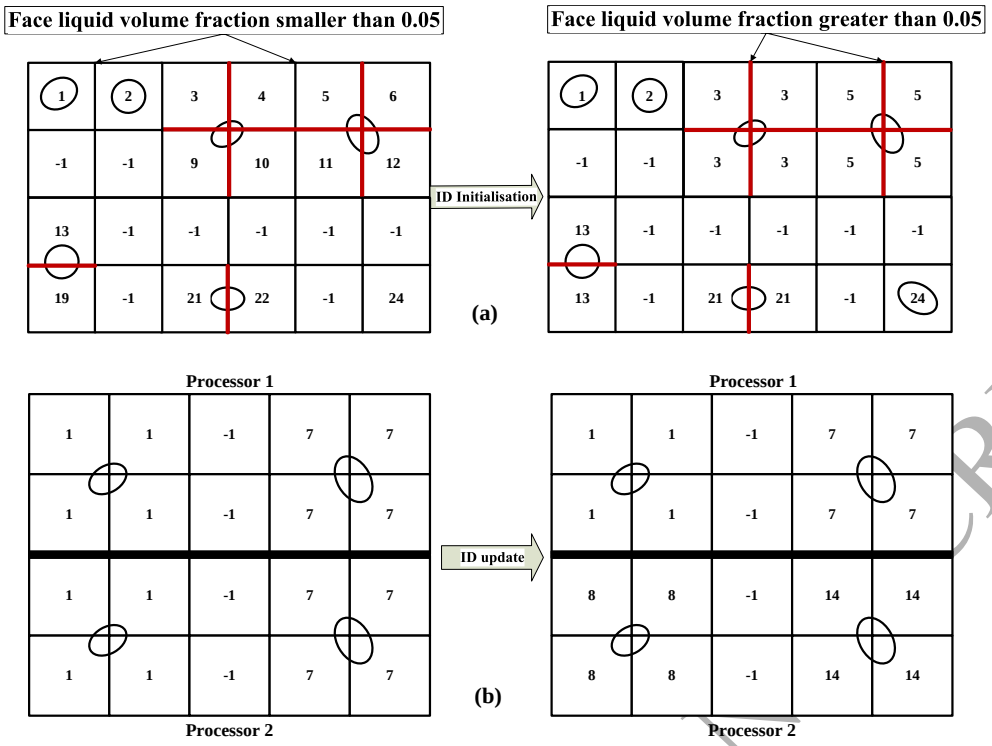

Figure 3: (a) ID initialisation of liquid structures. Adjacent liquid-containing cells sharing a cell face with $\partial_l \geq 0.05$ (marked in red) are combined to form contiguous liquid structures. The ID of a combined liquid structure is changed to be the same as the associated cell bearing the smallest ID. An individual cell containing liquid but not having a liquid containing neighbour is also identified as an individual liquid structure. Cells of zero liquid volume fraction are tagged with -1. (b) Updating of the liquid structure IDs across the computational domain. Each processor adds the maximum ID received from its higher ranked neighbour to its local liquid structures to ensure the uniqueness of every liquid structure in the domain.

2.7. Droplet Extraction Procedure (DEP)

In parallel computing mode, another important point that should be considered is the preservation of liquid structures that are on or approaching processor patches. This is because when a liquid structure moves from one processor domain to another, it is possible for it to be broken into droplets that are then erroneously extracted from the domain by the DEP. This procedure identifies liquid structures smaller than a pre-defined volume threshold, extracts and converts them to spherical droplets (by assigning $\alpha_l = 0$ to corresponding cells in the

VOF domain) that are injected into the Lagrangian domain. This situation is illustrated in Figure 4.

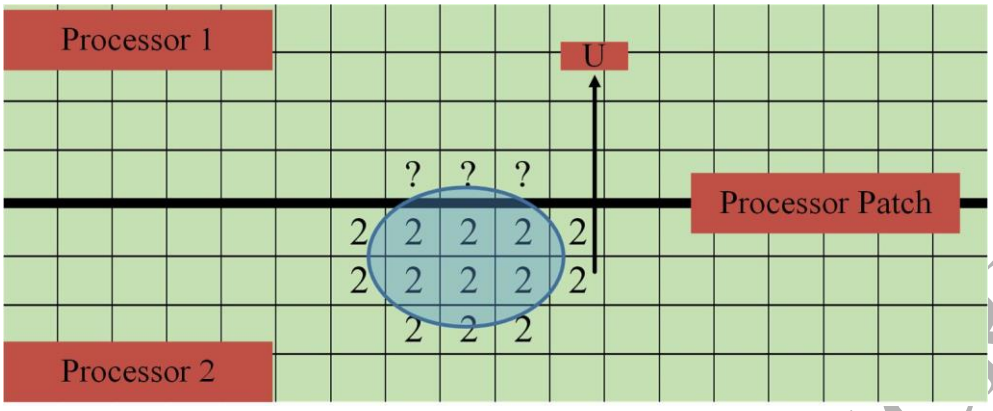

Figure 4: A liquid structure (ID=2) which is crossing the processor patch with a velocity vector U . The portion that could be erroneously extracted is tagged with question marks.

When a liquid structure crosses the processor patch, one cell in processor 1 will experience an increase in liquid volume fraction. Initially, as the liquid content might be too small to occupy this cell and there are no neighbours with $\alpha_l > 0.05$, the liquid contained would be recognised by the DEP as a suitable candidate for liquid structure-droplet conversion if a threshold of one cell volume was defined. Consequently, the entire liquid structure shown in Figure 4 would be non-physically extracted and transferred into same size Lagrangian droplets. These droplets could have a volume smaller than or equal to the volume of the first host cell in processor 1, and the size of computational time step largely governs the rate at which volume fraction increases in this cell. The degree of this problem is increasingly noticeable when high temporal resolution is required, especially when running LES.

A protection procedure is thus developed and implemented to tackle this problem. It simply stores IDs of all cells that are on processor patches in a Hash-table as different keys. These "keys" are triggered to locally deactivate the DEP when a liquid structure is detected to infect processor patch cells. The DEP therefore only applies to extract small liquid structures

that are not on or in close proximity to process patches. One disadvantage of such method is that it is dependent on the number and location of processor patches. Liquid structures suitable for VOF-LPT conversion which are in the vicinity of processor patches are not extracted such that this can be a source of error for the subsequent LPT simulation. However, contribution of this error can be negligible due to the small number of processor patch cells as compared to cells in the decomposed domain especially for high level parallel applications. Finally, properties of all the extracted liquid structures are sent to the master processor by its slaves and are stored in three Hash-tables (Table 1) designated to record liquid structures' (pre-LPT droplets) IDs and their corresponding x_P , U_p and R_p .

Table 1: Hash-tables storing properties of pre-LPT droplets.

Hash-table 1		*Hash-table 2*		*Hash-table 3*	
Droplet ID	R_p	*Droplet ID*	X_P	*Droplet ID*	U_p
1	R_1	*1*	(x_1, y_1, z_1)	*1*	(u_1, v_1, w_1)
2	R_2	*2*	(x_2, y_2, z_2)	*2*	(u_2, v_2, w_2)
3	R_3	*3*	(x_3, y_3, z_3)	*3*	(u_3, v_3, w_3)
....	....	....	....	....	....

The implementation of the identification and extraction procedure has a limited influence on the parallel efficiency of the original VOF code in OpenFOAM, simply because it does not increase the communications between processors as the assembly of liquid structures is strictly restricted within each processor domain. The use of the protection procedure eliminates the need to assemble liquid structures across processors, which would be computationally expensive. The complete droplet identification process is schematically shown in Figure 5.

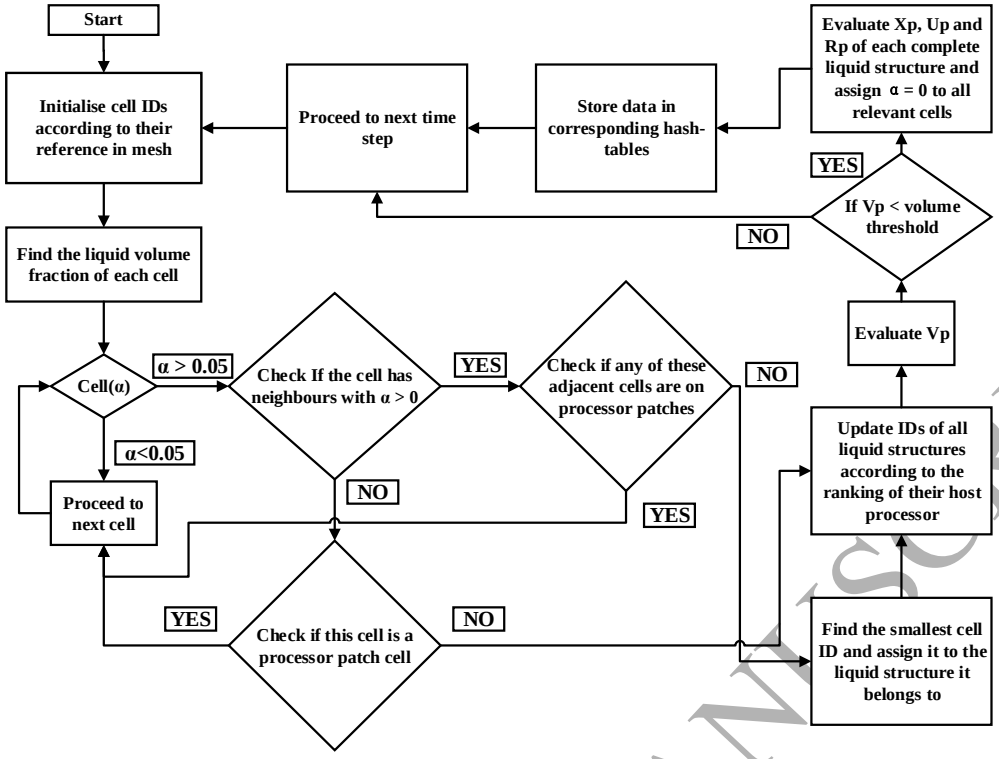

Figure 5: Flow process for parallel droplet identification algorithm.

In the present study, the LPT droplets are not converted back to VOF liquid structures when the mesh is sufficiently fine for VOF simulation. This decision is made based on considering the complexity and accuracy of the reversed VOF-LPT transition. Specifically, it is difficult to determine which and how many cells to which liquid volume fraction would be assigned to represent one Lagrangian droplet. Also, converting Lagrangian droplets into VOF ligaments without taking into account how the liquid interface of the ligaments is distributed across various VOF cells could be a large source of error especially for the modelling of sub-grid physics. Implementing algorithms to accurately describe the LPT-VOF transition would require development of a new sub-grid Eulerian model which is beyond the scope of this study. In addition, executing such a complex algorithm in transient LES simulations could be impractical because only marginally higher accuracy would be gained at the expense of greatly increased computing time.

Before the publication of this work, the capabilities of the developed parallel droplet identification and extraction procedures have been demonstrated in Ghiji *et al.*'s work [56, 57] (up to 512 CPUs) to be able to quantify the effects of grid resolution on the number of secondary droplets generated due to the breakup of liquid jet.

2.8. Droplet injector

The next step in VOF-LPT coupling is the injection of droplets transferred by the DEP to the Lagrangian domain. The injection process must satisfy conservation laws in order to preserve the accuracy of coupling. This involves developing a utility able to read information from the three Hash-tables and transform them into Lagrangian droplets, preserving their mass, momentum and positions. A new automatic injector with such capabilities is developed as part of the coupling method. This injector scans every entry in the three Hash-tables at run-time and acquires the volume, position and velocity of the droplets to be injected. The process diagram shown in Figure 6 schematically depicts how this injector works.

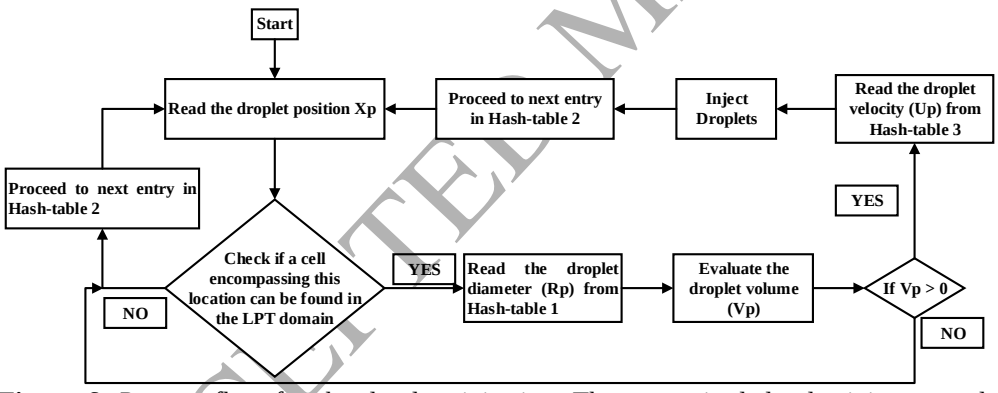

Figure 6: Process flow for the droplets injection. The customised droplet injector reads information from the Hash-tables and converts it into droplets that are injected into the LPT simulation. Numerical approach

Based on the recent work of Ghiji *et al.* [57], the governing equations are solved by OpenFOAM using a Pressure Implicit with Splitting of Operator (PISO) algorithm. In each Eulerian time-step, the intermediate velocity field (U^*) in the VOF simulation is first

evaluated using a semi-discretised momentum equation which consists of a predicted velocity field, an explicit pressure correction term and a surface tension source term [58]:

$$U^* = \frac{H(U_{n-1})}{a} - \frac{1}{a}\nabla p_{n-1} + S_{surface} \tag{30}$$

where U_{n-1} and p_{n-1} are velocity and pressure fields mapped from the LPT solution obtained from the previous Eulerian time-step.

Divergence of the predicted velocity field is then substituted into the two-phase pressure equation of which the detailed derivation can be found in our previous work [59]:

$$\begin{cases} \dfrac{\alpha_l}{\rho_l}\left[\psi_l \dfrac{\partial p_{n-1}}{\partial t} + U_{n-1}\cdot\nabla(\rho_l)\right] + \dfrac{1-\alpha_l}{\rho_g}\left[\psi_g \dfrac{\partial p_{n-1}}{\partial t} + U_{n-1}\cdot\nabla(\rho_g)\right] \\ + \\ \nabla\cdot(U^*) \\ = 0 \end{cases} \tag{31}$$

Equation (30) is then recalculated to update the velocity field using the solution of equation (31). The evaluated pressure (p_n) and velocity (U_n) fields are then mapped to the LPT simulation to initiate a similar pressure-velocity coupling procedure (comprising the particle force source term $S_{particle}$) within the same Eulerian time-step:

$$U^* = \frac{H(U_n)}{a} - \frac{1}{a}\nabla p_n + S_{particle} \tag{32}$$

$$\frac{1}{\rho_g}\left[\psi \frac{\partial p_n}{\partial t} + U_n\cdot\nabla(\rho_g)\right] + \nabla\cdot(U^*) = 0 \tag{33}$$

Finally, the calculated pressure (p_{n+1}) and velocity (U_{n+1}) fields are mapped to the VOF simulation to initiate the next Eulerian time-step.

To solve the pressure-velocity coupling equations, a bounded Normalised Variable (NV) Gamma differencing scheme [60] with a blending factor of 0.2 is used for the convection terms and an interface compression scheme (CICSAM) [47] for high resolution

interface capturing. A conservative, second order scheme (Gauss linear corrected) is employed for Laplacian derivatives and a second order backward discretisation scheme is adopted for temporal terms.

3. TEST CASE

A comparison of the RCM and a statistical coupling approach (SCA) is presented in this section. The test case, as outlined in the work of Grosshans *et al*.[40], concerns the atomisation of a simple diesel spray injected from a nozzle which has a diameter (d) of 100 µm. The liquid jet has an initial injection velocity of 500 m/s following a top hat profile at the nozzle exit, which corresponds to a Reynolds number of 15000 and a jet Weber number of 1.2×10^6. The ambient is filled with air of which the density is 14.8 kg/m3. The ambient pressure is 52 bar and the liquid and gas have a density ratio of 10 and a viscosity ratio of 46.

Comment [HY1]: Response to reviewer 3' 1st comment.

3.1. Comparison of VOF simulation

Similar to Grosshans *et al*.'s statistical coupling approach, a VOF simulation is first run to determine the position of the coupling region. In this case, the coupling region is placed where the averaged liquid volume fraction along the centre line of the jet is lower than 0.25 indicating the onset of major jet breakup. The liquid volume fraction is averaged at every time-step using OpenFOAM's runtime field-Averaging utility and the averaging time relates to the jet crossing the domain 15 times. A Cartesian equidistant grid duplicating the highest resolution case (cell size = 0.05d) considered in Grosshans *et al*.' work [40] is generated and employed for the VOF simulation..

Figure 7 shows that the averaged liquid volume fraction becomes lower than 0.25 at z=24d in the RCM-VOF simulation and at z=26d in the Grosshans-VOF simulation [40]. Although two cases depict similar trend along the penetration axis, the RCM-VOF method predicts a higher jet disintegration intensity after 5d from the tube exit since the averaged liquid volume fraction is slightly lower than Grosshans-VOF's prediction. The deviation

between two simulations can be attributed to the different numerical approaches employed (RCM-VOF: Finite Volume Method, Grosshans-VOF: Finite Difference Method). Specifically, the FVM based VOF is able to capture shear layer instabilities most probably generated due to either the Kelvin-Helmholtz mechanism [61] (Figure 8) or 2D Tollmien-Schlichting instability [62] while the FDM based VOF only predicts a smooth exiting jet within several diameters downstream of the tube exit (readers can refer to Figure 15 in ref. [40]). Other factors include the use of different numerical and time integration schemes between the RCM-VOF simulation and the Grosshans-VOF simulation.

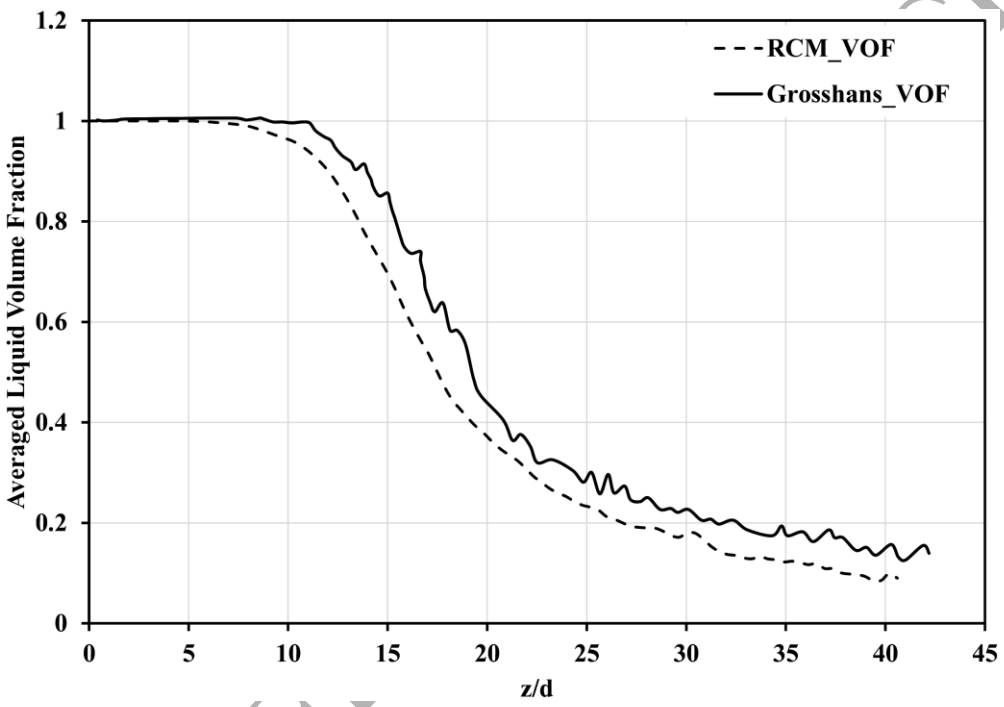

Figure 7: Plotted average liquid volume fraction along the jet centre line for the RCM-VOF simulation and the Grosshans-VOF simulation [40]. The distance from nozzle exit is non-dimensionalised by nozzle diameter d.

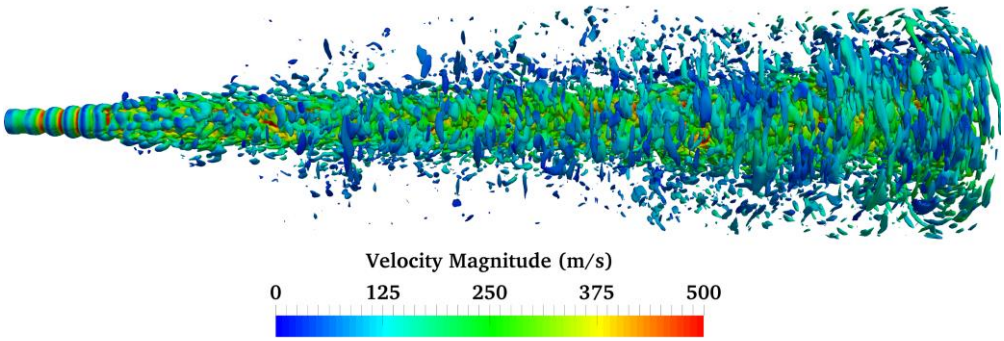

Figure 8: Contour plot of liquid volume fraction represented by an $\alpha = 0.1$ isosurface after the jet has penetrated the domain for 15 times. The liquid volume fraction is coloured by velocity magnitude.

3.2. Comparison of Coupling simulation

In order to make a consistent comparison in terms of the droplet size distribution between the RCM and the SCA, the coupling region in the RCM simulation is placed after z=29.6d which is also the position of the coupling layer in the Grosshans-SCA simulation [40]. The coupling region extends the length of the computational domain to 41d which is kept the same as the computational domain used in [40]. Finally, the RCM is employed in the VOF-LPT coupling region to identify liquid structures suitable for VOF-LPT conversion and transfer them into the LPT simulation. The simulation is performed for an extended time equivalent to the jet crossing the entire VOF-LPT domain 10 times. The liquid jet isosurface together with the converted droplets are displayed in Figure 9. The droplet cloud visualisation and analysis of the size distribution reveal that most converted droplets have a diameter between 1 μm and 10 μm, which is consistent with the droplet size distribution obtained by Grosshans *et al*. [40] as shown in Figure 10. However, significantly larger quantity of small droplets (3-8 μm) are identified and extracted by the RCM while SCA produces a droplet size PDF which shifts more to larger droplet diameters. On the one hand, these differences can be attributed to the slightly higher breakup intensity predicted by the RCM-VOF method. On the other hand, indistinguishably converting all liquid structures sampled at the coupling layer without applying a volume threshold leads to the generation of more large Lagrangian

droplets in the SCA simulation. Since the size of these droplets do not necessarily satisfy the requirement that a Lagrangian droplet must be smaller than the local grid size, it is more difficult to ensure numerical stability in the SCA than in the RCM.

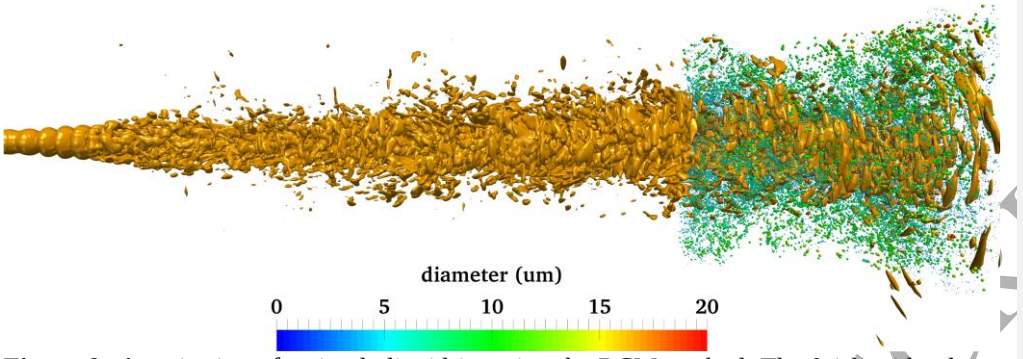

Figure 9: Atomisation of a simple liquid jet using the RCM method. The 0.1 liquid volume isosurface is coloured in brown while the converted Lagrangian droplets are scaled and coloured according to their diameters.

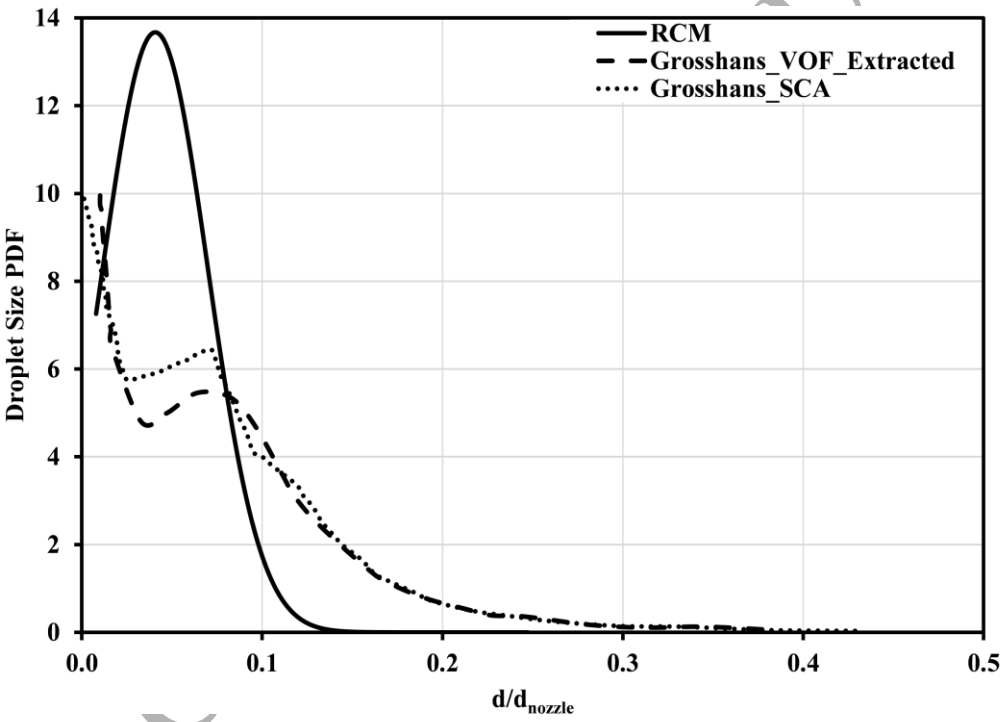

Figure 10: Comparison of predicted droplet size distributions between RCM and SCA. The size distribution calculated for the extracted VOF droplets from the Grosshans-VOF simulation is also added to demonstrate the difference between the RCM and SCA. The droplet diameter is non-dimensionalised by the nozzle diameter.

The effects of different decomposition strategies on the identification and extraction of droplets are demonstrated using 16, 32, 64, 96, 128 and 196 CPU processors. The simulation time is equivalent to the jet crossing the entire domain 10 times. A scotch method is employed to ensure that each processor domain is assigned with equal numbers of mesh elements. The numerical instability in time integration is eliminated by fixing the time step size at 1.4×10^{-9} s for all simulations. As shown in Figure 11(a), decomposing the computational domain with increasing number of CPUs has a diminishing effect on the droplet identification and conversion procedures. Moreover, the size distributions of converted droplets under different decomposing conditions display negligible difference as depicted in Figure 11(b). These comparisons demonstrates RCM's good adaptability to high level parallel simulations.

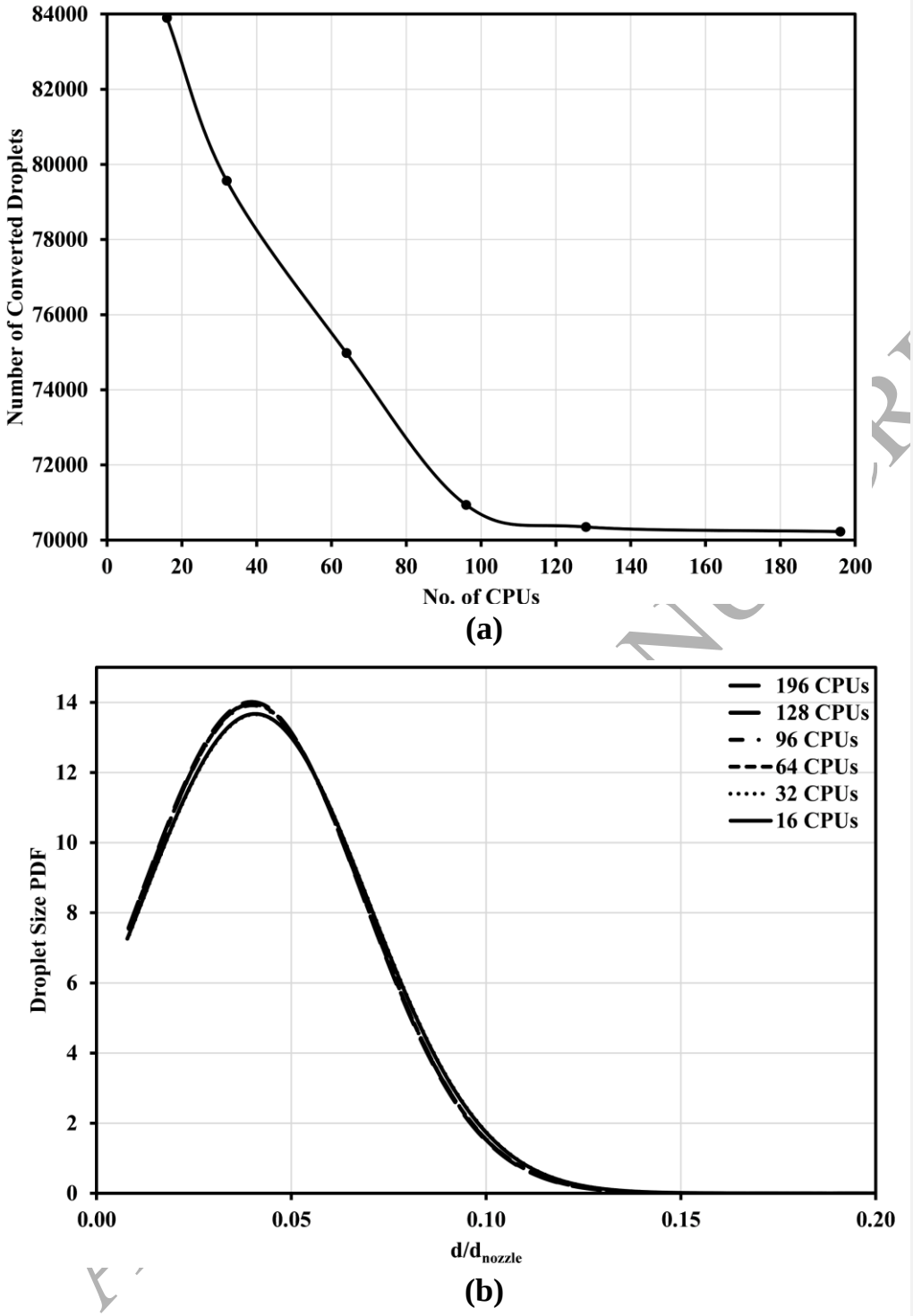

Figure 11: Comparison of the quantity of converted droplets (a) and their size distributions (b) using different number of CPUs.

4. COUPLING OF IN-NOZZLE FLOW TO SPRAY ATOMISATION

In this section, the application of the RCM is further extended to couple the in-nozzle flow with the primary and secondary spray atomisation. Firstly a pure VOF simulation is performed to determine the location and size of the VOF-LPT coupling region. Secondly the simulation of a real diesel spray from in-nozzle flow to secondary atomisation with transient VOF-LPT coupling is presented. The simulation is run until 200 μs after start of injection (ASOI).

4.1. Boundary conditions

Experimental conditions given in the work of Goldsworthy *et al.* [4], relevant for a non-evaporative spray from a sharp edged orifice are simulated. The ambient volume is non-reactive and initially filled with compressed air at 30 bar. Boundary conditions for the simulation cases are similar to the experimental conditions in Goldsworthy *et al.* [4] and Ghiji *et al.* [57] given in Table 2. However, in the absence of direct measurement, sac pressure is assumed to increase from chamber pressure (30 bar) to 850 bar after 50 μs then to 1200 bar after a further 25 μs then constant at 1200 bar to the end of simulation at 200 μs. This assumption is to some extent arbitrary but is made based on published data that the sac pressure increases rapidly during needle opening [63-65]. For instance, Moon *et al.* [63] found that the quasi-steady state jet velocity was reached when the needle was only elevated to 17% of the maximum lift. The ramp is chosen to give an approximate estimation of pressure variation due to needle dynamics. The reduced pressure rise rate in the second 25 μs is adopted to avoid numerical instabilities. This sac pressure ramp is same as that used by Ghiji *et al.* [57].

Table 2: Boundary conditions for spray injection corresponding to the 200 μs simulations. Nozzle diameter is used as the characteristic length.

Parameter	Value
Injection pressure	1200 bar
Nozzle diameter (D)	0.25mm

Nozzle length	1.6mm
Nozzle index factor (K_S)	0
Fuel	Diesel
Fuel density	832 kg/m^3
Gas	Compressed air
Density ratio	42
Fuel kinematic viscosity	2.5226×10^{-6} m^2/s
Surface tension	0.03 N/m
Temperature (Fuel and Ambient)	298 K
Chamber pressure	30 bar
Cavitation number	1.025
Fuel Reynolds number	7000≤Re≤47000

The cavitation number C is calculated from

$$C = \frac{P_{injection} - P_{vapour}}{P_{injection} - P_{ambient}} \tag{34}$$

$$\mathrm{Re}_l = \frac{\rho_l U_l D}{\mu_l} \tag{35}$$

4.2. Computational grid

The simulations comprise an injector and a fixed volume chamber. The injector grid is designed to include an inlet, a sac and a nozzle while the chamber mesh is shaped as a conical cylinder allowing a smooth transition of a fine grid in the nozzle to a relatively coarse grid at the end of the chamber. The geometry configuration of the computational domain is shown in Figure 12.

To achieve high resolution, mesh elements of 0.15 μm (1.5 times of the gas phase Kolmogorov scale and one-fifth of the liquid phase Kolmogorov scale [57]) are distributed in the nozzle where the in-nozzle flow separation, flow detachment and turbulent fluctuations are captured. The grid quality and resolution in the primary atomisation region (within 12D from the nozzle exit) are kept consistent with the finest grid employed in Ghiji *et al.*'s study [57]. To solve the problem that overly refined mesh can lead to the generation of excessive

quantity of sub-micron droplets, the cell size is proportionally increased from 0.15 μm at the nozzle exit to $\Delta x = \Delta y = \Delta z = 210$ μm at the end of the chamber, with a growth rate of 1.02 along penetration axis. The maximum cell size of 210 μm is related to the finest grid used for a LPT-LES simulation of a diesel spray in Jangi *et al.* [26]. In total, 25 million hexahedral cells are used to discretise the computational domain.

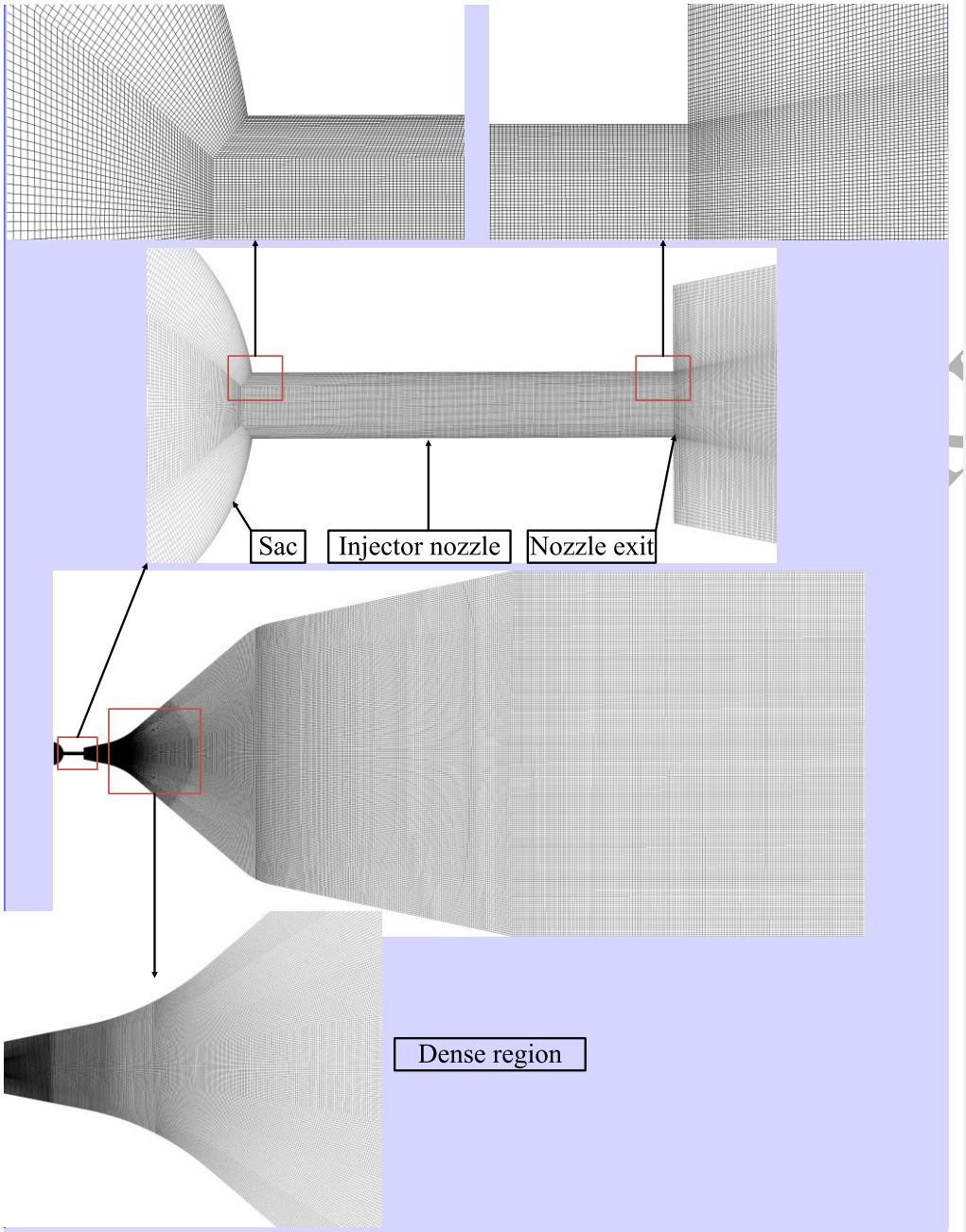

Figure 12: Computational grid design. Enlarged views are shown for the grid design at the nozzle entrance, in the nozzle hole, at the nozzle exit and in the dense region where the transition from fine grid to coarse grid starts. The total number of cells are 25 million and smallest cell size is 0.15 µm.

Comment [HY2]: Response to reviewer 3's 2nd comment.

The injector is initially filled with fuel up to the nozzle exit such that air is not present in the region near the nozzle entrance and the start of injection occurs shortly after the start of

simulation. The VOF simulation is initiated with the boundary configurations provided in Table 3, corresponding to Figure 13. The maximum Courant-Friedrichs-Lewy (CFL) number is set to 0.2, which gives an average time step size of 1.2×10^{-9} s.

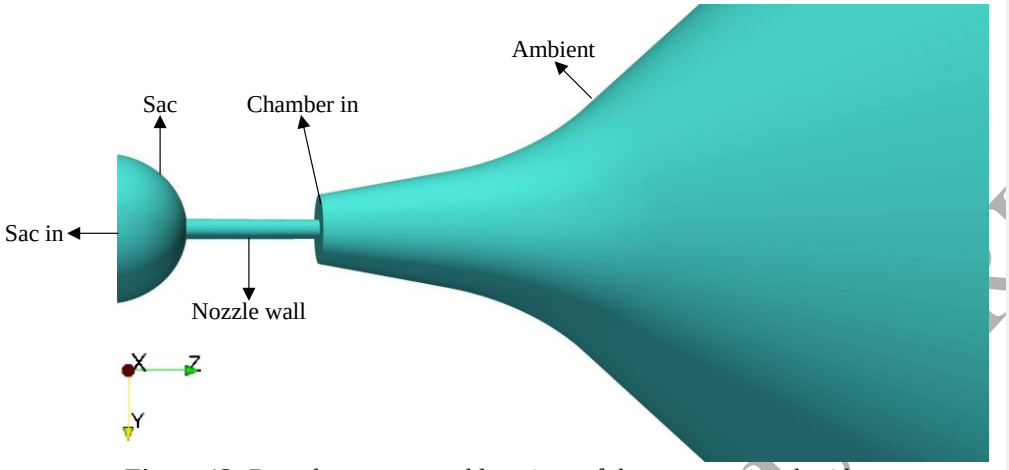

Figure 13: Boundary names and locations of the computational grid.

Table 3: Boundary configurations for the computational grid.

Boundary	Value
Sac in	Pressure inlet 30-1200 bar in 200 μs
Sac	No-slip and zero gradient (adiabatic)
Nozzle wall	No-slip and zero gradient (adiabatic)
Chamber in	No-slip and zero gradient (adiabatic)
Ambient	Non-reflective pressure boundary with a reference 30 bar

The simulation is performed on a computer cluster only using 96 core i7 (3.4GHz) processors which are granted a total of 96GB physical memory.

Prior to the generation of the LPT grid, a pure VOF simulation is run to 200 μs ASOI. The volume fraction plots for the VOF simulation at onset of major jet breakup (90 μs ASOI) and at end of simulation (200 μs ASOI) are shown in Figure 14 (a). Major jet breakup is designated to occur from 90 μs ASOI when the liquid core starts to disintegrate. The coupling region is then placed after 52D from the injector inlet to encompass the entire region where an intact liquid core ($\alpha_l < 0.5$) does not exist at 90 μs and 200 μs ASOI, as shown in Figure 14 (b).

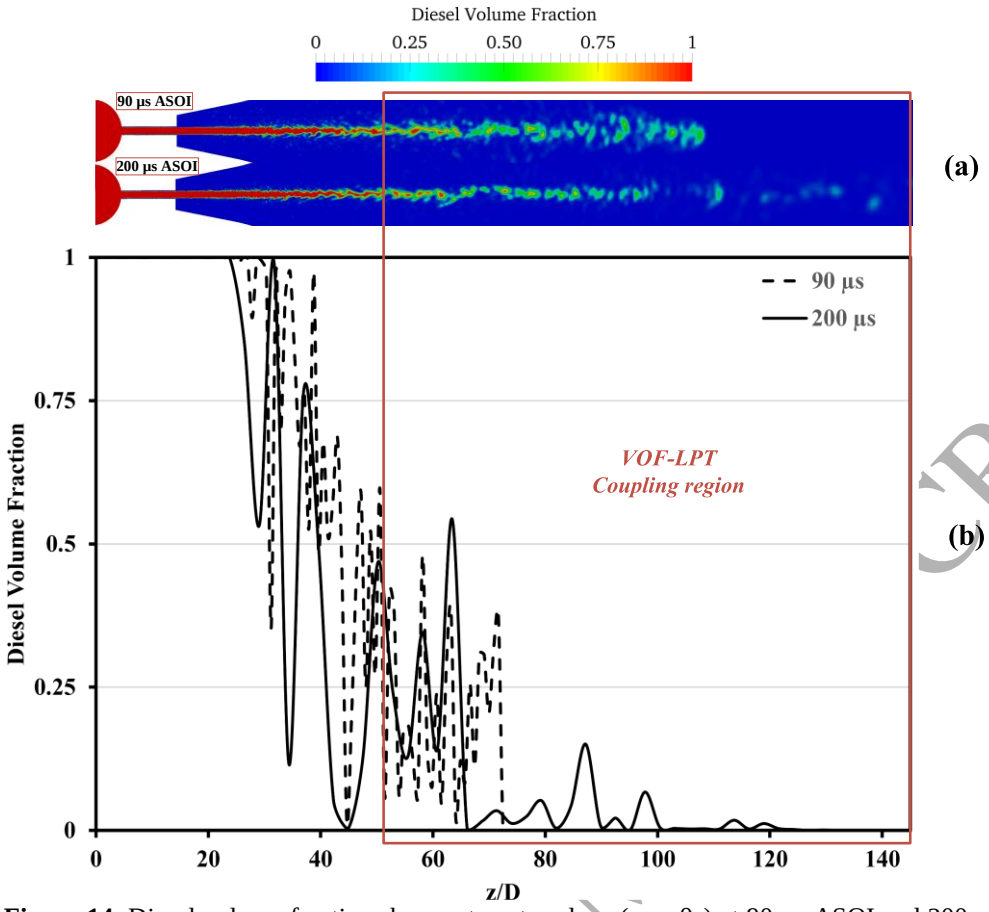

Figure 14: Diesel volume fraction shown at centre plane ($x = 0$) at 90 µs ASOI and 200 µs ASOI (a), and the instantaneous variation of diesel volume fraction along the penetration axis at 90 µs ASOI and 200 µs ASOI (b). The VOF-LPT coupling region is placed after 52D from the injector inlet.

Based on the pure VOF simulation, the computational domain is separated into two regions respectively for the VOF and LPT simulations. These two simulations are connected by the coupling region where the two-way mapping of velocity and pressure fields is deployed. It should be pointed out that the overlapping VOF-LPT regions have identical mesh design and elements distribution in order to ensure high fidelity field mapping between two simulations. After the grid separation, the minimum and maximum cell sizes in the coupling region are Δz_{min} = 58 µm (start of coupling region) and Δz_{max} = 140 µm (end of coupling region). As shown in Figure 15, the length and the maximum diameter of the

conical section of the mesh in the chamber are based on the spray angle and spray penetrating length reported in Bong [33]. The coupling region is extend further 55 nozzle diameters from the point of maximum liquid penetration to avoid potential boundary effects imposed by the right end of the coupling region. All dimensions are non-dimensionalised by the nozzle diameter.

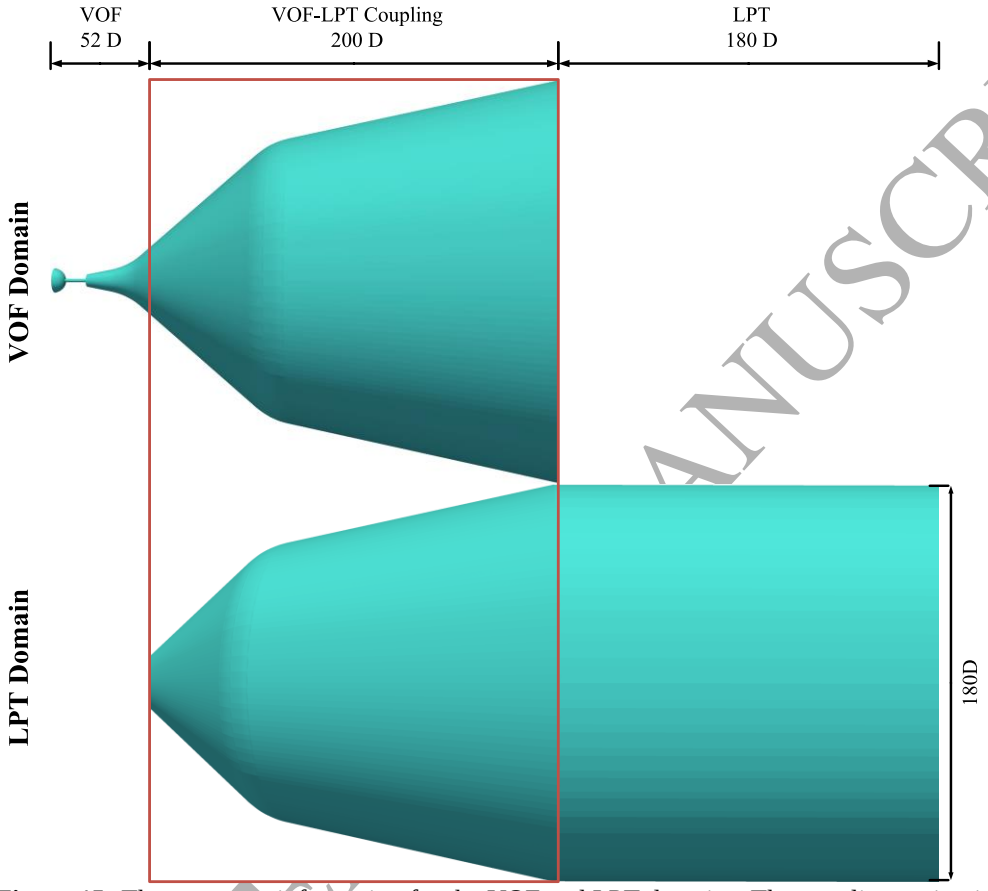

Figure 15*:* The geometry information for the VOF and LPT domains. The coupling region is enclosed in red box. The size of the LPT domain is determined from the results reported in Bong [33]. All dimensions are normalised by the nozzle diameter (D).

4.3. Pure VOF simulation

In Figure 16 (a-d), the emerging spray is represented by a 0.5 diesel volume fraction isosurface coloured by turbulent kinetic energy while the fluid in the sac is coloured by diesel volume fraction displayed at the $x = 0$ plane. The 'mushroom' like leading edge is formed

due to aerodynamic forces exerted by the compressed air ahead of the spray tip. The disintegration of this mushroom-like structure at the periphery due to aerodynamic shear provides an initial mechanism for droplet formation. At 25 ASOI, toroidal transverse waves start to develop on the liquid-gas interface upstream of the mushroom structure. These spanwise waves could be potentially generated due to either Kelvin-Helmholtz instability or 2D tollmien-Schlichting instability as recently reported by Shinjo and Umemura from DNS for a low Reynolds number [62]. In-nozzle cavitation is observed to initiate from the sharp nozzle inlet and the growth of cavitation pockets all the way up to the nozzle exit together with liquid-wall shear contribute to the development of surface disturbances. This is evident after 35 µs ASOI with the appearance of 3D surface instabilities (breakup) increasing in quantity and magnitude with time. It is also noticed that once the flow has separated from the nozzle wall due to cavitation induced hydraulic flip, the quantity and magnitude of surface instabilities are diminished. This can be attributed to the minimised effects of wall shear on the liquid surface. Nevertheless, the absence of wall shear and the decrease in effective flow area lead to increased injection velocity, which is reflected by apparent increase in interfacial turbulent kinetic energy at 45 µs ASOI.

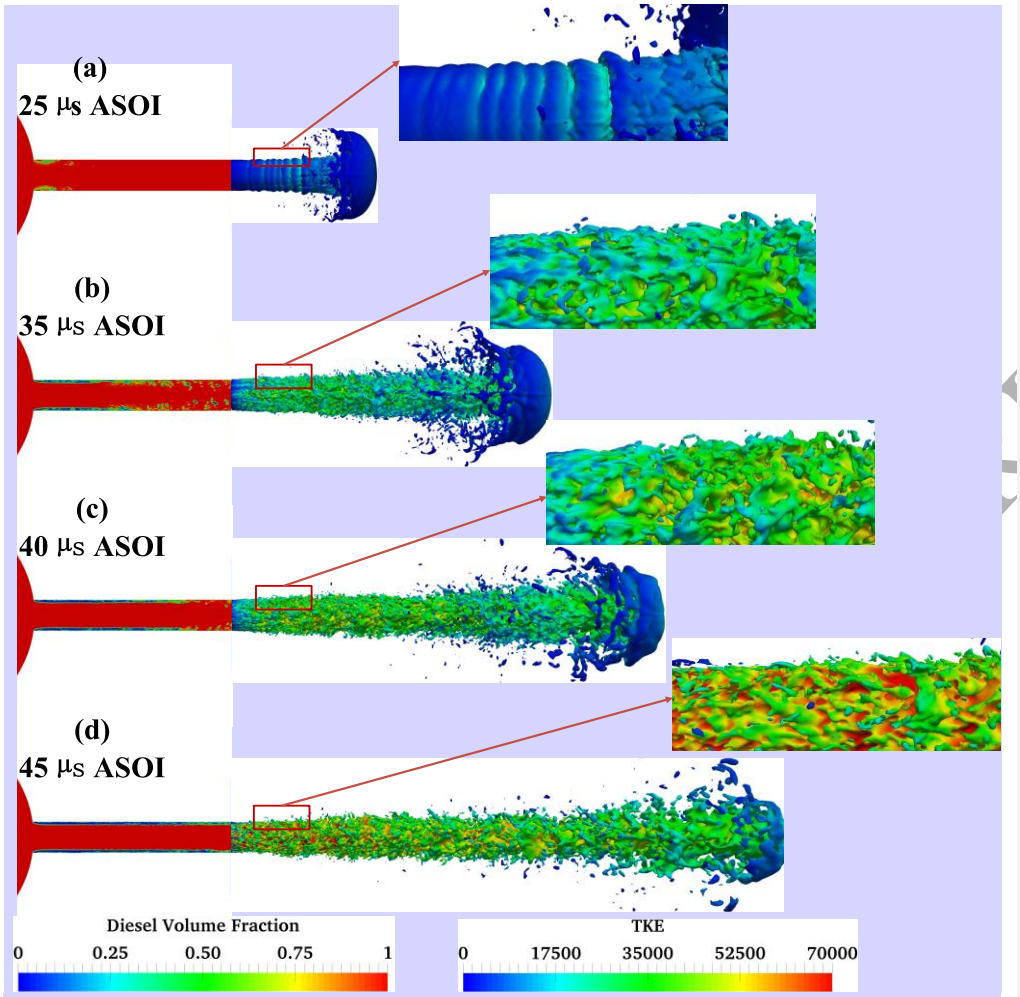

Figure 16: Evolution of in-nozzle and liquid jet turbulent structures at 25, 35, 40 and 45 µs ASOI. In images a-d, in nozzle flow is coloured by diesel volume fraction displayed at $x = 0$ plane; liquid-gas isosurface of 0.5 is used to represent the emerging spray coloured by turbulent kinetic energy. Detailed evolution of surface instabilities are shown in the enlarged images.

Comment [HY3]: Response to reviewer 3' comment.

In this study, a mesh sensitivity analysis has not been done because for VOF-LES methods, increasing mesh refinement always leads to an increasingly high resolution of interphase capturing. Unlike the Reynolds averaged models, such a trend persists until the mesh is fine enough for a DNS simulation. On the other hand, the quality of the LES simulation is assessed by evaluating the resolved kinetic energy as a fraction of the estimated total kinetic energy in the computational domain, as reported by Yu *et al.*[59]. The resolved

kinetic energy is obtained from the Root Mean Square of the velocity components and consecutively time averaged over the simulation. It is then divided by the estimated total kinetic energy (resolved kinetic energy + contribution of the sub-grid kinetic energy) to quantify how much kinetic energy is resolved by the grid. As shown in Figure 17, the chamber flow around and at the liquid-gas interface is very well resolved since the resolved kinetic energy is more than 90% of the total kinetic energy [66]. This indicates that turbulent disturbances causing spray breakup in the chamber are sufficiently captured by the grid. However, a decrease in the measured simulation resolution (only 50%-75% of kinetic energy is resolved) is observed in the nozzle wall boundary layer and in the liquid core region within 10 diameters upstream and downstream of the nozzle exit. In these regions, acceleration of liquid spray and the presence of liquid-gas velocity shear in the nozzle generate significant small scale turbulences that cannot be sufficiently resolved by the grid. The smallest turbulent length scale in these regions can become equivalent to the gas phase Kolmogorov scale which was evaluated to be 0.1 µm by Ghiji *et al.* [57]. To resolve all turbulences at this scale, the grid size must be less than half of the gas phase Kolmogorov scale [58] and only DNS can be employed to obtained a fully resolved flow. Nevertheless, performing a DNS of the entire spray breakup is computationally impractical at such a high Reynolds number and therefore is not considered in this study.

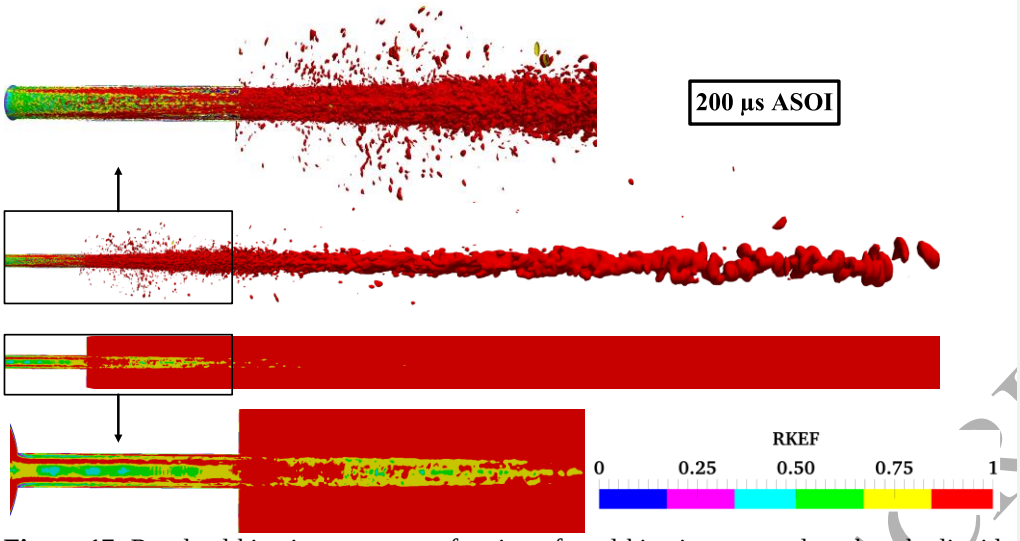

Figure 17: Resolved kinetic energy as a fraction of total kinetic energy plotted at the liquid isosurface ($\alpha_l = 0.05$) and at the $x = 0$ plane. Detailed distribution of this fraction in the injector nozzle is also shown in the enlarged views. The fraction of resolved kinetic energy and its contour plot are time averaged over the simulation.

4.4. VOF-LPT coupling

4.4.1. Droplet identification and extraction

The demonstration of the droplet identification and extraction procedure is performed in the first time step of the VOF-LPT coupling simulation, 0.4 nanosecond after 90 µs ASOI. During this period, 1913 liquid structures discretised by less than 5 cells and smaller than 20% of their host cells are identified. The physics of these liquid structures can no longer be accurately predicted by the VOF-LES method and therefore they are extracted from the VOF domain, inserted and modelled in the LPT domain as depicted in the 0.05 liquid volume isosurface plots of Figure 18 (a) and (b). As shown in the histograms of Figure 18 (a) and (b), the number of VOF droplets that are discretised by less than 5 cells decreases significantly (more than 90%) after droplets identification and extraction.

(a)

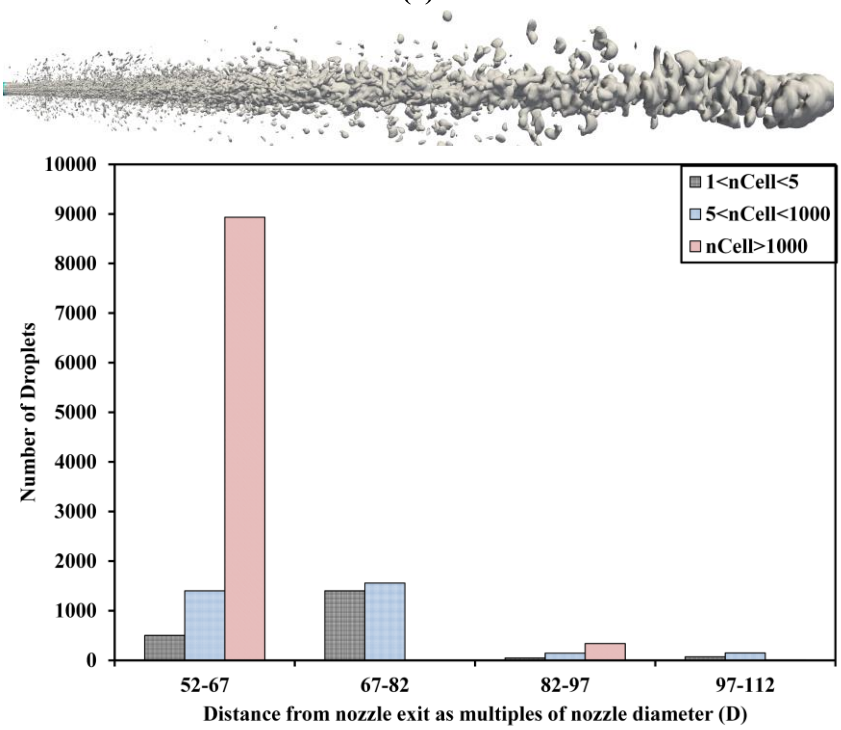
10000
9000
8000
7000
6000
5000
4000
3000
2000
1000
0
Number of Droplets
1<nCell<5
5<nCell<1000
nCell>1000
52-67
67-82
82-97
97-112
Distance from nozzle exit as multiples of nozzle diameter (D)

(b)

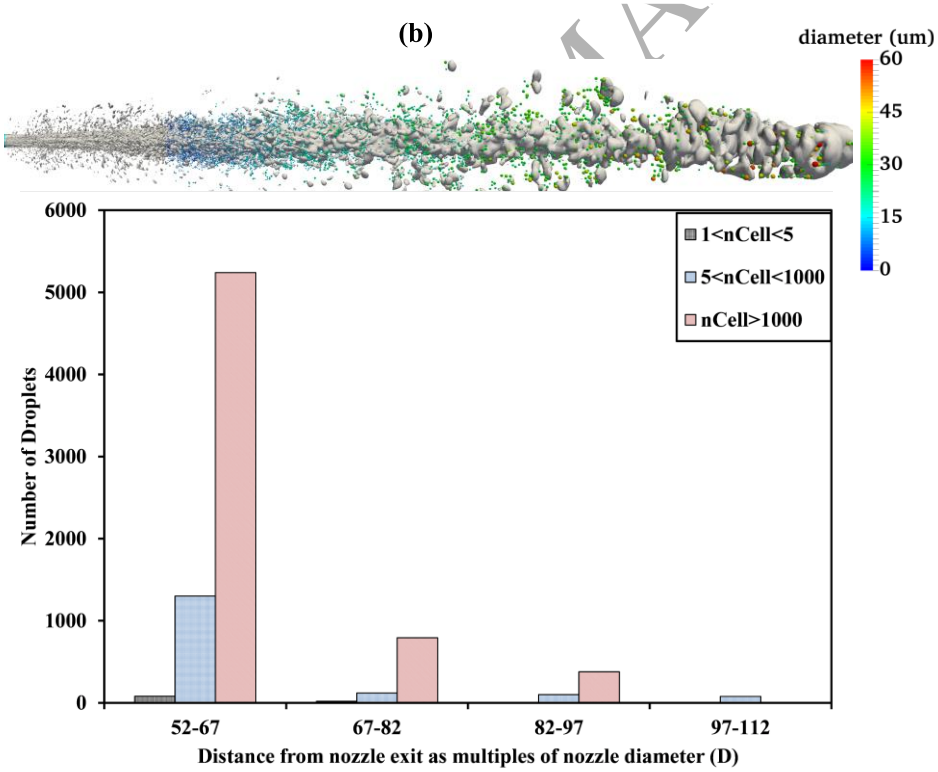
diameter (um)
60
45
30
15
0
6000
5000
4000
3000
2000
1000
0
Number of Droplets
1<nCell<5
5<nCell<1000
nCell>1000
52-67
67-82
82-97
97-112
Distance from nozzle exit as multiples of nozzle diameter (D)

Figure 18: Contour plots of 0.05 liquid volume isosurface before (a) and after (b) the first time-step of the VOF-LPT coupling simulation. In image (b), the converted Lagrangian droplets are scaled and coloured according to their diameters. Also, numbers of VOF droplets captured by 1 to 5 cells and by greater than 5 cells before (a) and after (b) the first time-step are statistically represented using histograms. More than 90% of the droplets captured by less than 5 mesh cells have been extracted and converted to Lagrangian droplets.

4.4.2. Secondary atomisation

Major spray breakup is simulated to occur from 90 μs, hence the simulation of the secondary atomisation is initiated from 90 μs. It is linked to the primary atomisation through the RCM. The two-way field coupling of pressure and velocity fields allows the effects of in-nozzle flow separation, flow detachment and turbulence to be conveyed to the LPT simulation and the effects of LPT droplet-gas interaction to be reflected on the VOF simulation. The field coupling is performed at every Eulerian time-step during the VOF-LPT simulation. The field mapping results between two simulations in the overlap region at 200 μs can be seen in Figure 19 to be indistinguishable. It preserves the field information in the mapping process and the high-fidelity exchange of field data between two simulations enables high resolution coupling of VOF-LPT.

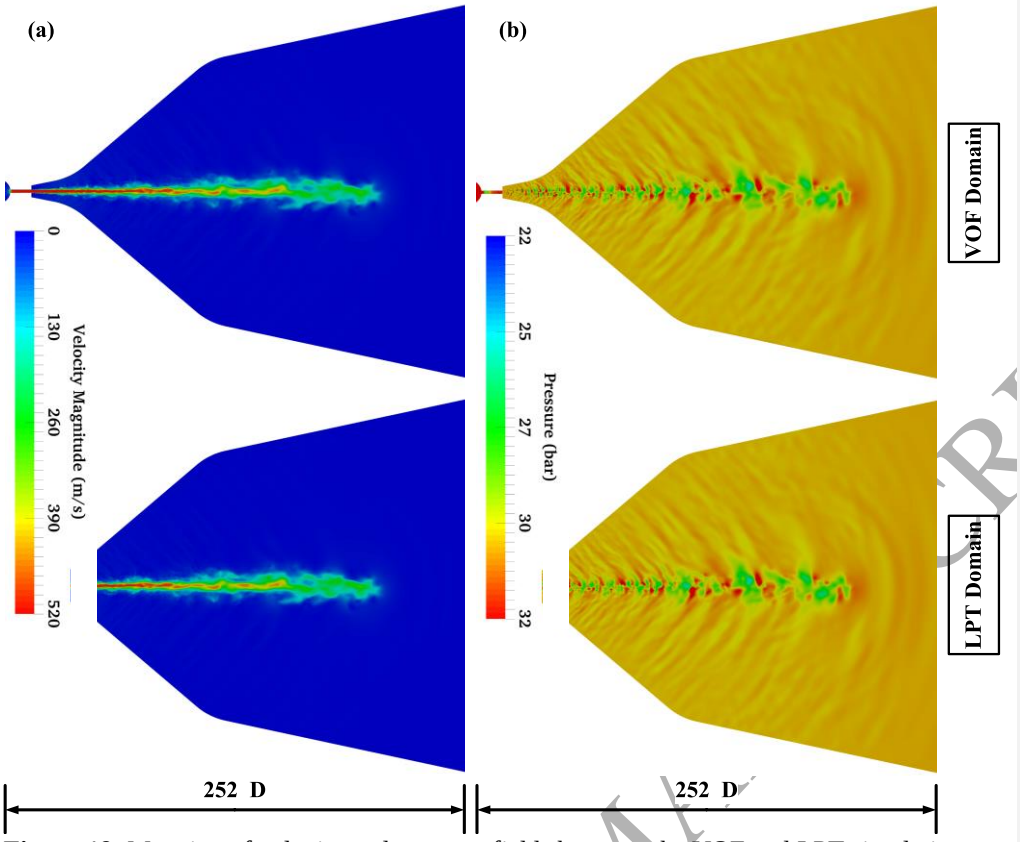

Figure 19: Mapping of velocity and pressure fields between the VOF and LPT simulations at 200 µs ASOI. The pictures on the left (a) show contour plots of velocity magnitude at the centre plane ($x = 0$), while the pictures on the right (b) display the pressure at the centre plane.

The atomised diesel jet, the transferred Lagrangian droplets, and the remaining VOF phase interface geometry at 100 and 200 µs ASOI are shown in Figure 20. At 100 µs ASOI, stripped off liquid structures from the liquid core start to be converted into Lagrangian droplets in the major breakup region. These large parent droplets undergo secondary breakup that generates child parcels which have a diameter smaller than 30 µm. At 200 µs ASOI, approximately 0.9 million droplets have been transferred into the Lagrangian simulation while the unconverted liquid structures (Blobs) are still modelled in the VOF domain. The diameters of these fine droplets range from 0.8 µm up to 74 µm, which indicates a wide spectrum of droplet diameters attributed to the RCM. With the intensifying droplet-gas

interaction, the turbulent effects of the flow on the droplets at the sub-grid level increases the spacing between droplets and produces a more dispersed spray cloud. At the spray tip, interaction of the compressible air and the secondary droplets leads to the formation of a mushroom like penetrating spray. Also, recirculation of the droplet clouds (circled in red) is observed to occur in the middle section of spray. This is mainly attributed to droplets entrainment of which the modelling is enabled by the implementation of the LES stochastic droplet dispersion model. The breakup of secondary droplets is statistically represented by the droplet-size distribution in Figure 21. The size distribution at four instants continuously shifts to the left due to the atomisation of secondary droplets which is governed by the KH-RT model. Detailed analysis of the effects of the implementation of these two models is beyond the scope of the present work and will be considered in future work.

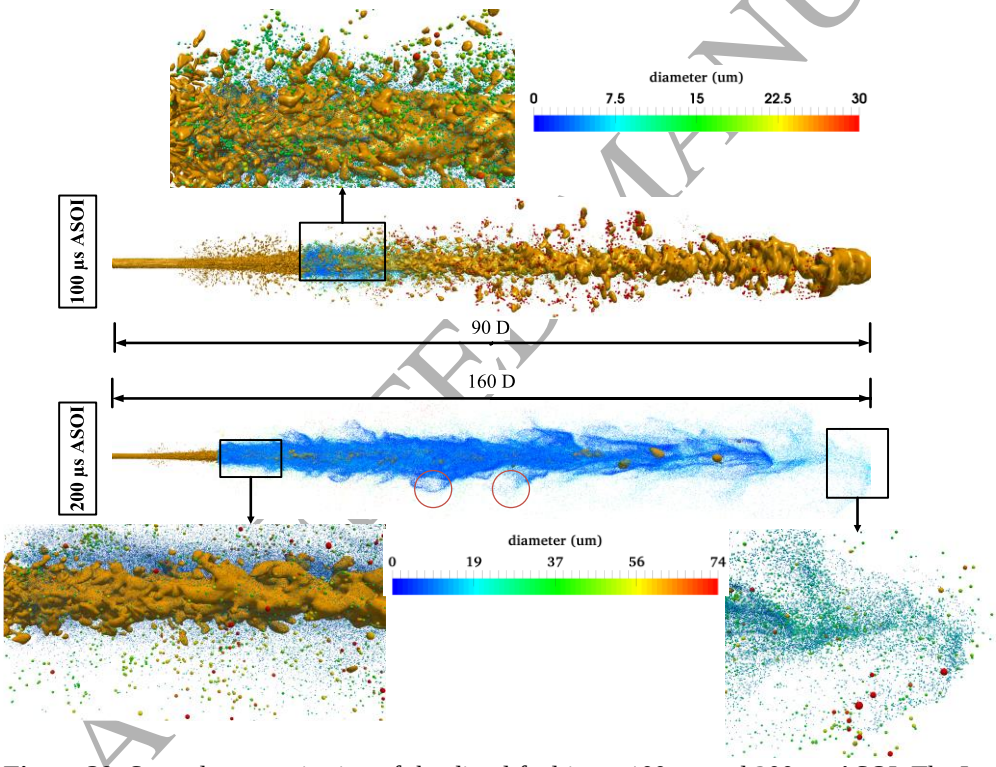

Figure 20: Secondary atomisation of the diesel fuel jet at 100 µs and 200 µs ASOI. The Iso-surface ($\alpha = 0.05$) of the liquid jet is coloured brown and the Lagrangian droplets are scaled

and coloured according to their diameters. The squared areas are enlarged for better clarity and the circled areas are where entrainment of spray clouds occurs.

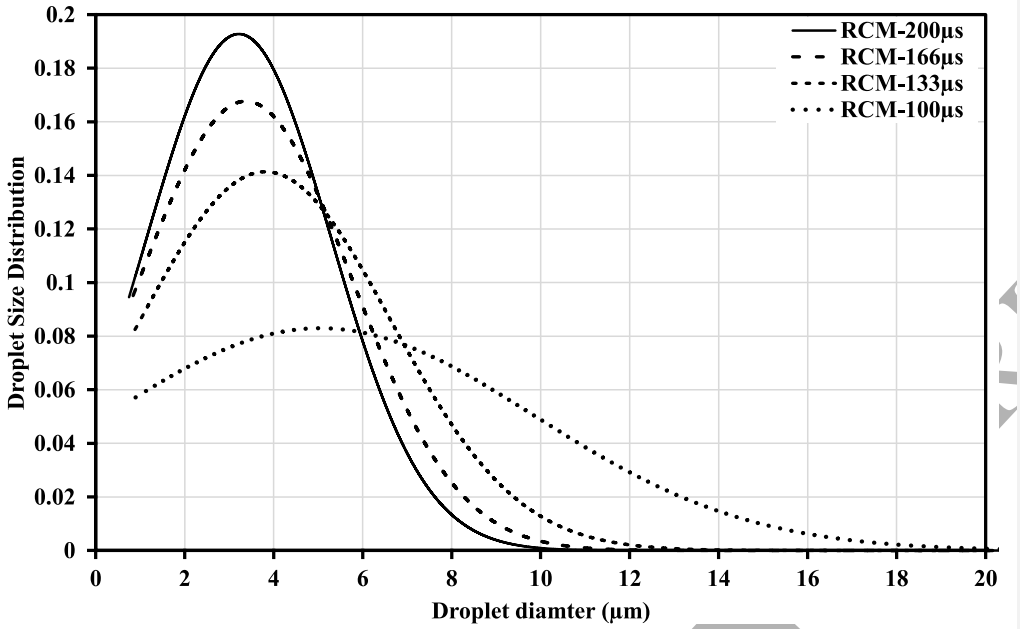

Figure 21: Comparison of Lagrangian-droplet-size distribution at four instants (t =100, 133, 166 and 200 µs after start of injection).

5. CONCLUSIONS

In this paper a parallel VOF-LPT coupling procedure between an Eulerian-Eulerian Volume of Fluid and an Eulerian-Lagrangian Lagrangian Parcel Tracking is presented. The coupling procedure links the VOF and LPT simulations with parallelised droplet identification, extraction and insertion procedures and a region coupling method that are deployed in a VOF-LPT transition region. The use of two identical grids in the transition region enables high-resolution coupling of velocity and pressure fields between VOF-LES and LPT-LES, which is independent of the turbulence model. The implementation of KH-RT secondary breakup, LES Stochastic Turbulence Dispersion and Stochastic Trajectory Collision models allows the use in the LPT simulation of the parcel assumption as a better replacement for the point particle tracking approach. The coupling procedure is first

compared with a statistical coupling approach of which the applications are strictly restricted to the modelling of static sprays. The comparison demonstrates that:

- The parallel processing procedure for the identification and extraction of droplets from VOF simulation has negligible effects on the droplet statistics with different domain decomposition strategies
- The region coupling method is able to predict the transient spray evolution from a liquid jet to dispersed secondary droplets with high fidelity, which is attributed to the implementation of a conservative transient region coupling procedure.

The capability of the coupling approach is further demonstrated by application to the modelling of a real diesel spray from a nozzle with a sharp entrance, from which it was shown that:

- The sub-gird LES dispersion model and the trajectory collision model enable the modelling of droplets entrainment in the middle section of the spray, as well as the formation of a mushroom droplet cloud at the spray tip.
- The KH-RT secondary breakup model allows the simulation of secondary atomisation of the droplets, which produces a penetrating spray with a decreasing average droplet diameter.

Overall, the parallel droplet identification, extraction and insertion procedures together with the region coupling method are shown to be applicable to the simulation of complex diesel injection processes. Further validation of the proposed coupling procedure will be considered in future work.

Comment [HY4]: Response to reviewer 3' 4th comment.

ACKNOWLEDGEMENT

Significant support was received from the Australian Maritime College in terms of the access to the high performance computer clusters and installation of OpenFOAM. The

authors express their gratitude to Luciano Mason and Zhi Quan Leong for their support and suggestions.

REFERENCES

1. Gorokhovski, M. and M. Herrmann, *Modeling primary atomization.* Annu. Rev. Fluid Mech., 2008. **40**: p. 343-366.

2. Fath, A., C. Fettes, and A. Leipertz. *Investigation of the diesel spray break-up close to the nozzle at different injection conditions*. in *Fourth International Symposium on Diagnostics and Modeling of Combustion in Internal Combustion Engines, Kyoto, Japan, JSME*. 1998.

3. Goldsworthy, L., N. Ashraf, and P. Brandner, *Development of a high pressure chamber for research into diesel spray dynamics.* Australian Journal of Mechanical Engineering, 2009. **7**(2): p. 15-34.

4. Goldsworthy, L., C. Bong, and P. Brandner, *Measurements of diesel spray dynamics and the influence of fuel viscosity using PIV and shadowgraphy.* Atomization and Sprays, 2011. **21**(2).

5. Kastengren, A.L., et al., *Time-resolved X-ray radiography of sprays from engine combustion network spray a diesel injectors.* Atomization and Sprays, 2014. **24**(3).

6. Sharma, P. and T. Fang, *Spray and atomization of a common rail fuel injector with non-circular orifices.* Fuel, 2015. **153**: p. 416-430.

7. Xue, Q., et al., *Eulerian CFD Modeling of Coupled Nozzle Flow and Spray with Validation Against X-Ray Radiography Data.* SAE International Journal of Engines, 2014. **7**(2014-01-1425): p. 1061-1072.

8. Villiers, E.d., D. Gosman, and H. Weller. *DETAILED INVESTIGATION OF DIESEL SPRAY ATOMISATION USING QUASI-DIRECT CFD SIMULATION (Spray Technologies, Atomization)*. in *The... international symposium on diagnostics and*

modeling of combustion in internal combustion engines. 2004. 一般社団法人日本機械学会.

9. Hirt, C.W. and B.D. Nichols, *Volume of fluid (VOF) method for the dynamics of free boundaries.* Journal of computational physics, 1981. **39**(1): p. 201-225.
10. Herrmann, M. *A dual scale volume-of-fluid approach for modeling turbulent phase interface dynamics*. in *Proceedings of the Summer Program*. 2014.
11. Bianchi, G.M., et al., *Improving the knowledge of high-speed liquid jets atomization by using quasi-direct 3d simulation*. 2005, SAE Technical Paper.
12. Löhner, R., C. Yang, and E. Oñate, *On the simulation of flows with violent free surface motion.* Computer Methods in Applied Mechanics and Engineering, 2006. **195**(41): p. 5597-5620.
13. Reddy, R. and R. Banerjee, *GPU accelerated VOF based multiphase flow solver and its application to sprays.* Computers & Fluids, 2015. **117**: p. 287-303.
14. Grosshans, H., et al., *Sensitivity of VOF simulations of the liquid jet breakup to physical and numerical parameters.* Computers & Fluids, 2016. **136**: p. 312-323.
15. Sussman, M., P. Smereka, and S. Osher, *A level set approach for computing solutions to incompressible two-phase flow.* Journal of Computational physics, 1994. **114**(1): p. 146-159.
16. Herrmann, M., *A balanced force refined level set grid method for two-phase flows on unstructured flow solver grids.* Journal of Computational Physics, 2008. **227**(4): p. 2674-2706.
17. Sussman, M. and E.G. Puckett, *A coupled level set and volume-of-fluid method for computing 3D and axisymmetric incompressible two-phase flows.* Journal of Computational Physics, 2000. **162**(2): p. 301-337.

18. Ménard, T., S. Tanguy, and A. Berlemont, *Coupling level set/VOF/ghost fluid methods: Validation and application to 3D simulation of the primary break-up of a liquid jet.* International Journal of Multiphase Flow, 2007. **33**(5): p. 510-524.

19. Arlov, D., J. Revstedt, and L. Fuchs. *A different approach for handling large bubbles in a square cross-sectioned bubble column combining Large Eddy Simulation with Lagrangian Particle Tracking*. in *6th International Conference on Multiphase Flow*. 2007.

20. Vallier, A., J. Revstedt, and H. Nilsson. *Procedure for the break-up of cavitation sheet*. in *4-th International Meeting on Cavitation and Dynamic Problems in Hydraulic Machinery and Systems, October, 26-28, 2011, Belgrade, Serbia*. 2011.

21. Vuorinen, V.A., et al., *Effect of droplet size and atomization on spray formation: A priori study using large-eddy simulation.* Flow, turbulence and combustion, 2011. **86**(3-4): p. 533-561.

22. Vreman, B., et al., *Two-and four-way coupled Euler–Lagrangian large-eddy simulation of turbulent particle-laden channel flow.* Flow, turbulence and combustion, 2009. **82**(1): p. 47-71.

23. Reitz, R.D., *Modeling atomization processes in high-pressure vaporizing sprays.* Atomisation Spray Technology, 1987. **3**: p. 309-337.

24. O'Rourke, P.J. and A.A. Amsden, *The TAB method for numerical calculation of spray droplet breakup*. 1987, SAE Technical Paper.

25. Oefelein, J.C., V. Sankaran, and T.G. Drozda, *Large eddy simulation of swirling particle-laden flow in a model axisymmetric combustor.* Proceedings of the Combustion Institute, 2007. **31**(2): p. 2291-2299.

26. Jangi, M., et al., *On large eddy simulation of diesel spray for internal combustion engines.* International Journal of Heat and Fluid Flow, 2015. **53**: p. 68-80.

27. Elghobashi, S., *On predicting particle-laden turbulent flows.* Applied Scientific Research, 1994. **52**(4): p. 309-329.

28. Apte, S., K. Mahesh, and T. Lundgren, *A Eulerian-Lagrangian model to simulate two-phase/particulate flows.* Annual Research Briefs, 2003: p. 161-171.

29. Apte, S., M. Gorokhovski, and P. Moin, *LES of atomizing spray with stochastic modeling of secondary breakup.* International Journal of Multiphase Flow, 2003. **29**(9): p. 1503-1522.

30. Li, Y. and S.-C. Kong, *Integration of parallel computation and dynamic mesh refinement for transient spray simulation.* Computer Methods in Applied Mechanics and Engineering, 2009. **198**(17): p. 1596-1608.

31. Reitz, R.D. and R. Diwakar, *Structure of high-pressure fuel sprays*. 1987, SAE Technical Paper.

32. Baumgarten, C., H. Lettmann, and G. Merker. *Modelling of primary and secondary break-up processes in high pressure diesel sprays*. in *CIMAC Congress*. 2004.

33. Bong, C.H., *Numerical and experimental analysis of diesel spray dynamics including the effects of fuel viscosity*. 2010, University of Tasmania.

34. Amsden, A., et al., *A computer program for chemically reactive flows with sprays, Los Alamos National Laboratory Rep*. 1989, LA-11560-MS.

35. Lefebvre, A., *Atomization and sprays*. Vol. 1040. 1988: CRC press.

36. Herrmann, M., *A parallel Eulerian interface tracking/Lagrangian point particle multi-scale coupling procedure.* Journal of Computational Physics, 2010. **229**(3): p. 745-759.

37. Tomar, G., et al., *Multiscale simulations of primary atomization.* Computers & Fluids, 2010. **39**(10): p. 1864-1874.

38. Burluka, A. and R. Borghi, *Development of a Eulerian model for the "atomization" of a liquid jet.* Atomization and sprays, 2001. **11**(6).

39. Desportes, A., *A combined Eulerian Lagrangian spray amortization (ELSA) in DI Diesel combustion: Fully coupled Euelrian/Lagrangian spray with ECFM-CLEH Combustion model.*

40. Grosshans, H., R.Z. Szász, and L. Fuchs, *Development of an efficient statistical volumes of fluid–Lagrangian particle tracking coupling method.* International Journal for Numerical Methods in Fluids, 2014. **74**(12): p. 898-918.

41. Befrui, B., et al., *Coupled LES Jet Primary Breakup-Lagrangian Spray Simulation of a GDi Multi-Hole Fuel Injector.* SAE International Journal of Fuels and Lubricants, 2015. **8**(2015-01-0943): p. 179-189.

42. Musculus, M.P. and K. Kattke, *Entrainment waves in diesel jets.* SAE International Journal of Engines, 2009. **2**(2009-01-1355): p. 1170-1193.

43. Open, C., *OpenFOAM user guide.* OpenFOAM Foundation, 2011. **2**(1).

44. De Villiers, E., A. Gosman, and H. Weller, *Large eddy simulation of primary diesel spray atomization*. 2004, SAE Technical Paper.

45. Brackbill, J., D.B. Kothe, and C. Zemach, *A continuum method for modeling surface tension.* Journal of computational physics, 1992. **100**(2): p. 335-354.

46. Mencinger, J. and I. Žun, *A PLIC–VOF method suited for adaptive moving grids.* Journal of Computational Physics, 2011. **230**(3): p. 644-663.

47. Ubbink, O., *Numerical prediction of two fluid systems with sharp interfaces*. 1997, University of London UK.

48. Ghiji, M., et al. *CFD Modelling of Primary Atomisation of Diesel Spray*. in *19th Australasian Fluid Mechanics Conference*. 2014.

49. Yoshizawa, A. and K. Horiuti, *A statistically-derived subgrid-scale kinetic energy model for the large-eddy simulation of turbulent flows.* Journal of the Physical Society of Japan, 1985. **54**(8): p. 2834-2839.

50. O'Rourke, P.J., *Statistical properties and numerical implementation of a model for droplet dispersion in a turbulent gas.* Journal of Computational Physics, 1989. **83**(2): p. 345-360.

51. Solsjö, R. and X.-S. Bai, *Injection of Fuel at High Pressure Conditions: LES Study*. 2011, SAE Technical Paper.

52. Kitaguchi, K., et al., *Optimization of breakup model using LES of diesel spray.* Atomization and Sprays, 2012. **22**(1).

53. Nordin, P., *Complex chemistry modeling of diesel spray combustion*. 2001: Chalmers University of Technology.

54. O'Rourke, P.J., *Collective drop effects on vaporizing liquid sprays*. 1981, Los Alamos National Lab., NM (USA).

55. Rusche, H., *Computational fluid dynamics of dispersed two-phase flows at high phase fractions*. 2003, Imperial College London (University of London).

56. Ghiji, M., et al., *Numerical and experimental investigation of early stage diesel sprays.* Fuel, 2016. **175**: p. 274-286.

57. Ghiji, M., et al., *Analysis of diesel spray dynamics using a compressible Eulerian/VOF/LES model and microscopic shadowgraphy.* Fuel, 2017. **188**: p. 352-366.

58. Jasak, H., *Error analysis and estimation for finite volume method with applications to fluid flow*. 1996.

59. Yu, H., et al., *Development of a compressible multiphase cavitation approach for diesel spray modelling.* Applied Mathematical Modelling, 2017. **45**: p. 705-727.

60. Jasak, H., H. Weller, and A. Gosman, *High resolution NVD differencing scheme for arbitrarily unstructured meshes.* International journal for numerical methods in fluids, 1999. **31**(2): p. 431-449.

61. Maidi, M., M. Lesieur, and O. Métais, *Vortex control in large-eddy simulations of compressible round jets.* Journal of Turbulence, 2006(7): p. N49.

62. Shinjo, J. and A. Umemura, *Surface instability and primary atomization characteristics of straight liquid jet sprays.* International Journal of Multiphase Flow, 2011. **37**(10): p. 1294-1304.

63. Moon, S., et al., *Effect of the number and position of nozzle holes on in-and near-nozzle dynamic characteristics of diesel injection.* Fuel, 2015. **150**: p. 112-122.

64. Papadopoulos, N. and P. Aleiferis, *Numerical modelling of the in-nozzle flow of a diesel injector with moving needle during and after the end of a full injection event.* SAE International Journal of Engines, 2015. **8**(2015-24-2472): p. 2285-2302.

65. Battistoni, M., C. Poggiani, and S. Som, *Prediction of the nozzle flow and jet characteristics at start and end of injection: transient behaviors.* SAE International Journal of Engines, 2015. **9**(2015-01-1850): p. 84-97.

66. Pope, S.B., *Ten questions concerning the large-eddy simulation of turbulent flows.* New journal of Physics, 2004. **6**(1): p. 35.